



RUI DANIEL DE OLIVEIRA

Bachelor in Science of Micro and Nanotechnologies Engineering

**OPTIMIZATION OF SELF-ASSEMBLED PARTICLE  
DEPOSITION FOR COLLOIDAL LITHOGRAPHY  
NANO/MICRO-PATTERNING**

Dissertation for the degree of Master in Micro and  
Nanotechnologies Engineering

Advisor:

Prof. Doutor Manuel João de Moura Dias Mendes, Assistant Professor,  
Departamento de Ciências dos Materiais, Faculdade de Ciências e  
Tecnologias da Universidade Nova de Lisboa

Co-Advisor:

Prof. Doutor Hugo Manuel Brito Águas, Assistant Professor,  
Departamento de Ciência dos Materiais, Faculdade de Ciências e  
Tecnologias da Universidade Nova de Lisboa

Chairperson: Prof. Doutor Rodrigo Ferrão de Paiva Martins

Rapporteur: Doutora Olalla Sanchez-Sobrado

Member: Prof. Doutor Manuel João de Moura Dias Mendes



FACULDADE DE  
CIÊNCIAS E TECNOLOGIA  
UNIVERSIDADE NOVA DE LISBOA

December, 2020



**Optimization of Self-Assembled Particle Deposition for Colloidal Lithography Nano/Micro-Patterning**

Copyright © Rui Daniel de Oliveira, 2020.

A Faculdade de Ciências e Tecnologia e a Universidade Nova de Lisboa tem o direito, perpétuo e sem limites geográficos, de arquivar e publicar esta dissertação através de exemplares impressos reproduzidos em papel ou de forma digital, ou por qualquer outro meio conhecido ou que venha a ser inventado, e de a divulgar através de repositórios científicos e de admitir a sua cópia e distribuição com objetivos educacionais ou de investigação, não comerciais, desde que seja dado crédito ao autor e editor



*“We can easily forgive a child who is afraid of the dark; the real tragedy of life is  
when men are afraid of the light.”*

– Plato



# Acknowledgments

Findos cinco anos de desafios, frustrações e novas descobertas, é com enorme prazer que agradeço aos grandes responsáveis pelo meu desenvolvimento enquanto ser humano e profissional desta muy nobre área científica.

Porque é impossível falar em nanotecnologia sem a menção do seu nome, o meu agradecimento especial ao Prof. Doutor Rodrigo Martins e à Prof.<sup>a</sup> Doutora Elvira Fortunato pela fundação do curso de Engenharia de Micro e Nanotecnologias, não descurando nunca a qualidade e brio pelas condições oferecidas aos seus alunos através dos centros de investigação CENIMAT|i3N e CEMOP.

Ao meu orientador, Prof. Doutor Manuel J. Mendes, agradeço sobretudo o acompanhamento e direção durante todo um período mais difícil do que o usual, desde o fornecimento da mais variada literatura ao aconselhamento sobre o próximo passo a dar. Agradeço ainda ao meu co-orientador Prof. Doutor Hugo Águas e aos investigadores Doutora Ana Mouquinho, Jenny Boane, Pedro Centeno, Sirazul Haque e Miguel Alexandre por todas as dicas, sugestões, conselhos e ideias, sem esquecer a valiosíssima ajuda na escrita do artigo de revisão e no trabalho de laboratório. Aos múltiplos professores que conheci e com quem aprendi, não poderei nunca estar de deixar grato porque em mim deixaram marcas e experiências que nunca poderei esquecer.

O meu agradecimento especial ainda, enquanto antigo membro da Comissão Organizadora das Jornadas Tecnológicas do DCM, Materiais 2019, ExpoFCT e de tantas outras iniciativas do departamento, às equipas com quem trabalhei, realçando a amizade, dedicação e todo o apoio incansável que a Sónia Soares e a Sara Oliveira sempre deram a estes projetos, à casa e aos alunos que desta fazem parte.

A minha vida académica não seria a mesma sem pessoas fantásticas que me acompanharam sempre em múltiplos desafios, e por isso para elas vai a minha gratidão. Em especial ao Miguel Amaral, pelos bons e pelos maus momentos, hoje e sempre *team got it*. À malta deste grandioso curso e muy nobre faculdade.

À autêntica e eterna família que aqui construí, que tanto cresceu e com quem tanto cresci: em especial os padrinhos Manuel Caetano e Joana Rodrigues, os afilhados Chico Ferreira, Michele dell’Erba, João Sousa e Cristiano Barardo, assim como a malta mais nova – são e sempre serão motivo dos maiores dos meus orgulhos. À minha CoPe, grupo de veteranos e a todos os meus caloiros, que sempre lutaram a meu lado pela definição deste conceito maravilhoso de fazer dos outros melhores pessoas. À anTUNiA, pela música e não só.

Aos que nunca deixaram de estar lá, desde sempre e para a vida continuarão. Ao Ricardo Arsénio, a minha eterna gratidão, pois se na vida temos um braço direito, este senhor esteve sempre lá presente para ser os dois. Ao Tiago Gouveia, Rita Gonçalves, Diogo Augusto e Andreia Baptista por continuarmos ao fim de tantos anos a criar memórias, juntos. Não poderia deixar de homenagear postumamente o Sr. Luiz Nunes, agradecendo também à D. Elizangela Socoloski e ao Sr. Antero Nogueira, por me ajudarem a crescer como profissional e como Homem.

Devo toda a minha gratidão, de grandeza inestimável, ao meu pai, mãe, irmãos, avós, família - pelos desafios superados juntos, pelas lágrimas, pelas alegrias. Por terem contribuído para aquilo que é a definição do meu carácter hoje. De hoje, e de sempre.

This work was supported via funding by FCT (Fundação para a Ciência e Tecnologia, I.P.) under the projects UIDB/50025/2020, Apolo (H220-LCE 2017-RES-RIA), SuperSolar (PTDC/NAN-OPT/28430/2017) and TACIT (PTDC/NAN-OPT/28837/2017).



# Abstract

Colloidal lithography (CL) is nowadays considered a preferential nano/micro-patterning method for photovoltaic structuring, as it is an inexpensive and highly scalable soft-lithography technique allowing nanoscale precision over indefinitely large areas. Photonic wavelength-sized structures are on the top of the list of solutions that can boost photovoltaic performance without significantly increasing cost, as they enable pronounced broadband anti-reflection, LT effects, and even self-cleaning functionality. In particular, recent research suggested that these micro-structures can boost not only the efficiency but also the stability of the emergent perovskite solar cell technology.

CL methods critically depend on the long-range ordered self-assembly that can be attained upon deposition of the particles' array used as a mask, which is performed via the Langmuir-Blodgett method. However, it is still challenging to achieve the desired deposition quality particularly with the preferential polystyrene colloids with wavelength-scale dimensions. This thesis is focused on tackling this challenge and in the optimization of the self-assembly deposition of polystyrene nanospheres monolayers onto flexible substrates, as a part of a full CL method for photonic-enhancement purposes in thin-film solar cells.

In this work, we report a breakthrough in our Langmuir-Blodgett (LB) method which prevents wavelength-sized particles from sinking into the aqueous sub-phase and spontaneously form the desired close-packed hexagonal monolayer. This was attained by using sodium dodecyl sulfate (SDS) to reduce the aqueous sub-phase surface tension and hence improve the air-water interface stability of polystyrene spheres of various diameters. The addition of SDS, with best results at 4.5 mg/l concentration, showed remarkable improvement on the self-assembly step, by avoiding the nanospheres sinking and by producing uniform high-quality monolayer films. The quality of the deposition was also improved by controlling the LB barrier closing rate and increasing the self-assembly work area, which resulted in fully patterned flexible substrates.

**Keywords:** Light-trapping in Photovoltaics, Photonic structuring, Colloidal lithography, Langmuir-Blodgett, Particle Self-assembly



## Resumo

A litografia coloidal é atualmente vista como método preferencial para a micro e nanopadronização de estruturas fotônicas, já que se revela de baixo custo e com potencial de aplicação a largas escalas. As nanoestruturas fotônicas estão no topo da lista de soluções que podem assegurar uma melhoria significativa na eficiência fotovoltaica sem aumento do custo, permitindo efeitos de anti reflexão, captura de luz e até de autolimpeza. Estudos recentes sugerem que este tipo de microestruturas poderá não só beneficiar a eficiência dos dispositivos como melhorar a estabilidade da tecnologia emergente de células solares de perovskita.

Esta técnica depende da área de automontagem ordenada que se obtém com a deposição de partículas coloidal como máscara, através de métodos como Langmuir-Blodgett. No entanto, revela-se difícil a deposição de partículas de poliestireno com dimensões da escala típica dos comprimentos de onda. Esta tese foca-se em ultrapassar este obstáculo e otimizar a deposição em substratos flexíveis, de modo a aplicar num método de litografia coloidal para o melhoramento fotónico de células solares de filme fino.

No decurso deste trabalho, reportamos a otimização do nosso método Langmuir-Blodgett (LB) de modo a prevenir que partículas mais pequenas se afundem, permitindo a formação de uma monocamada ordenada e com estrutura hexagonal, como desejado. Isto deve-se à dissolução de dodecil sulfato de sódio (SDS) na subfase aquosa de modo a reduzir a sua tensão superficial, melhorando a estabilidade das esferas na interface ar-água. A adição de SDS, a uma melhor concentração de 4.5 mg/l, revelou melhorias significativas na automontagem, evitando o afundamento das nanoesferas e permitindo a produção de uma monocamada de elevada qualidade para a deposição. A qualidade da deposição foi também otimizada através do controlo do fecho de barreiras e do aumento da área dedicada à automontagem, resultando em substratos totalmente depositados.

**Palavras-chave:** Aprisionamento de Luz em Fotovoltaico, Estruturação Fotónica, Litografia Coloidal, Langmuir-Blodgett, Organização Espontânea



# Table of Contents

Acknowledgments.....	vii
Abstract .....	ix
Resumo.....	xi
Table of Contents.....	xiii
List of Figures .....	xv
List of Tables .....	xvii
Abbreviations .....	xix
Symbols.....	xxi
Motivation and Objectives .....	xxiii
Chapter I: Introduction .....	1
1.1. Photovoltaic light-trapping technologies .....	1
1.2. Colloidal lithography approach .....	3
Chapter II: Experimental .....	7
2.1. Langmuir-Blodgett trough .....	7
2.2. Substrate preparation .....	7
2.3. Aqueous sub-phase preparation .....	7
2.4. PS nanospheres preparation.....	7
2.5. PS nanospheres deposition.....	8
2.6. Characterization - SEM and ImageJ.....	8
Chapter III: Results and Discussion .....	9
3.1. PS nanospheres deposition (1.3 $\mu\text{m}$ size) .....	11
3.2. PS nanospheres self-assembly (below 1 $\mu\text{m}$ size).....	12
3.3. PS nanospheres deposition (below 1 $\mu\text{m}$ size) .....	16
3.4. Results Overview .....	25
Chapter IV: Conclusions and Future Perspectives .....	27
References .....	29
Appendices .....	35



# List of Figures

Figure 1.1.1 - Schematic drawings and SEM pictures of the samples obtained after the different steps of the TiO <sub>2</sub> nanostructure construction via CL: (a) a hexagonal array of colloidal PS spheres is patterned on the cell front, (b) O <sub>2</sub> dry etching, (c) TiO <sub>2</sub> is deposited, filling the inter-particle spaces, (d) sphere are removed leaving an array of semi spheroidal void-like features. The final TiO <sub>2</sub> structure, (e) uniformly covers the entire sample area. [39] .....	2
Figure 1.2.1 – 3D illustration of the self-assembly of colloidal particle structures forming a hexagonal close-packed array (also known as honeycomb), which results in the highest in-plane packing density – single particles tend to bond with others due to either physical, fluidic, external fields, or chemical force driving, from single, to small clusters to larger monolayers..	3
Figure 1.2.2 - Production of a colloidal monolayer using (a) a spin coating technique, (b) Doctor Blade trough, (c), and a Langmuir-Blodgett trough. ....	4
Figure 1.2.3 - Schematic of surfactant molecules and PS micelles in aqueous solution [61] .....	5
Figure 3.1 - Close-packing hexagonal geometry and the relation between the sphere size and the corresponding honeycomb structure with surrounding particles. ....	9
Figure 3.2 - Schematic diagram showing an arrangement of perfect hexagonally close-packed colloidal monolayer structure. The numbers inside each circle indicate its distance from the central sphere (between centroids). [70] .....	10
Figure 3.1.1 – (a,b) SEM images of the deposition of 1.3 μm PS nanospheres in PET-ITO using a conventional LB method; (c) Fast Fourier Transform of SEM image b (d) Radial profile plot of the FFT image: normalized integrated intensity as a function of distance (the number of spheres diameters) .....	11
Figure 3.2.1 – Top (left) and side-view (right) of a turbid self-assembly aqueous subphase, a condition observed for both 0.5 and 0.6 μm PS nanospheres - a sign of sinking colloidal particles and absence of interfacial monolayer formation .....	13
Figure 3.2.2 – Top and side views on the (a) floatation and self-assembly study for petri dish simulations on the deposition of 0.6 μm PS nanospheres on aqueous subphase without adding SDS and (b) adding a small concentration of SDS (4.5 mg/l). Turbid subphase and colloidal precipitation were observed within the conventional method, while the addition of a small amount of SDS developed bright colorful interfacial clusters, well defined in thickness and surface. ....	14
Figure 3.2.3 - Petri dish simulation of five different PS:ethanol proportions with 0.6 μm PS nanospheres: (a) 2:1; (b) 1:1; (c) 1:2; (d) 1:3; (e) 1:4 .....	15
Figure 3.3.1 - SEM images of the PS nanosphere size variation effect: (a,b) for 0.6 μm; (c,d) for 0.7 μm;.....	16
Figure 3.3.2 - Fast Fourier Transform of the SEM image and radial profile, respectively, for 0.6 (a,b) and 0.7 μm (c,d) PS nanospheres. ....	17
Figure 3.3.3 - SEM images of 0.6 μm PS nanospheres depositions with different solvents: (a,b) ethanol; (c,d) diacetone.....	18

Figure 3.3.4 - Fast Fourier Transform of the SEM image and radial profile for each solvent for 0.6 $\mu\text{m}$ PS nanospheres depositions - ethanol (a,b) and diacetone (c,d).....	19
Figure 3.3.5 - SEM images of 0.6 $\mu\text{m}$ PS nanospheres depositions using a 1:3 proportion in ethanol for different SDS concentrations in the subphase, respectively: (a,b) 3 mg/l; (c,d) 4.5 mg/l; (e,f) 6 mg/l.....	20
Figure 3.3.6 - Fast Fourier transform and radial profile of 0.6 $\mu\text{m}$ PS nanospheres depositions using a 1:3 proportion in ethanol for different SDS concentrations in the subphase, respectively: (a,b) 3 mg/l; (c,d) 4.5 mg/l; (e,f) 6 mg/l 6 mg/l .....	21
Figure 3.3.7 - Resulting typical defected substrates after the previous Langmuir-Blodgett 0.6 $\mu\text{m}$ PS nanospheres depositions: the achieving of a direction-oriented colorful pattern (see Google Drive video 8) areas indicate the attaining of a high-ordered layer, whereas ACS is higher; on the other hand, the more transparent/whitish areas indicate a low-quality deposition, which should reveal disordered nanosphere clusters, therefore, low substrate area uniformity.....	22
Figure 3.3.8 - 0.6 $\mu\text{m}$ PS nanospheres deposited substrates for strategy A (left) and strategy B (right): both the full barrier closing and the use of an ethanol underlayer produce substrates that show remarkable higher deposition substrate deposition coverages, with reduced defect signs. - see Google Drive video 8.....	23
Figure 3.3.9 - SEM images, fast Fourier transform and radial profile plot of the two additional approaches, respectively: (a,b,e,f) strategy A - barrier closing variation and (c,d,g,h) strategy B - ethanol underlayer deposition - for 0.6 $\mu\text{m}$ PS nanospheres depositions.....	24
Figure A.1 - ImageJ user interface.....	35
Figure A.2 - Cropped and scale SEM image in ImageJ.....	35
Figure A.3 - Image Threshold tool being performed onto the SEM image .....	36
Figure A.4 - (a) Binary mask of the SEM image array; (b) Fast Fourier Transform of the same image.....	36
Figure A.5 - Radial profile plot: a plot of normalized integrated intensities in the function of the distance as the number of full sphere diameters .....	37

## List of Tables

Table 3.3.1 – Effect of the addition of SDS (4.5 mg/l) in the monolayer self-assembly and substrate deposition for each PS nanosphere diameter .....	16
Table 3.4.1 - Overall results and performance indicators attained within this work...	25



# Abbreviations

**ACS** – Area Coverage Success

**CL** – Colloidal Lithography

**EtOH** – Ethanol

**FFT** – Fast Fourier Transform

**FFT-R** – Number of rings in the FFT

**FoM** – Figure of Merit

**IPA** – 2-propanol

**IR** – Infrared

**ITO** - Indium Tin Oxide

**LB** – Langmuir-Blodgett

**LT** – Light-Trapping

**NaCl** – Sodium Chloride

**PET** - Polyethylene terephthalate

**PS** – Polystyrene

**PSC** – Perovskite Solar Cell

**PV** – Photovoltaic

**RIE** – Reactive Ion Etching

**TCO** – Transparent Conducting Oxide

**TiO<sub>2</sub>** – Titanium Dioxide

**SAC** – Substrate Area Coverage

**SDS** – Sodium Dodecyl Sulfate

**SEM** – Scanning Electron Microscopy

**UV** – Ultraviolet



# Symbols

**$\mu\text{m}$**  – Micrometer

**nm** - Nanometer

**mm** –Millimeter

**cm** – Centimeter

**$\mu\text{L}$**  – Microliter

**L** – Liter

**mg** –Milligram

**mL** – Milliliter

**s** – Second

**I** – Intensity of the highest peak of the radial function

**R** – Regularity Ratio

**$W_{1/2}$**  – Width at half-height of the highest peak of the radial function



## Motivation and Objectives

The pursuit for ever more efficient, reliable, and affordable solar cells has increased demand for high-performance light-trapping strategies, capable of boosting their photovoltaic performance without significantly increasing costs [1–3]. It has been recently shown that the best-performing optical schemes make use of microstructures on the solar cells with features in the wavelength scale, as suggested by simulation work, therefore operating in the preferential wave-optical regime for photonic enhancement.

Colloidal lithography [4,5] is an incredibly promising approach for the micro and nanofabrication of photonic and photovoltaic applications. It is an especially interesting approach since it employs the use of a colloidal patterning mask, which can pattern any material yet not being affected by common limitations of other costly and complex structuring methods. With that in mind, this work aims to optimize the self-assembly and deposition of wavelength-sized nanospheres for colloidal lithography purposes. As this range of sizes does not usually show spontaneous air-water interface self-assembly, attaining a good, stable polystyrene nanosphere monolayer would be our first goal for colloidal lithography deposition.

The Langmuir-Blodgett method [6] combines rapid deposition times with versatility and scalability that are headmost characteristics for the fabrication of high-quality 2D and 3D crystalline films. Unlike other deposition methods like spin-coating or doctor blading, Langmuir-Blodgett resulting thin-films tend to show high-uniformity, in which the formation of a monolayer is more accurately assured. Specific parameters like the nanosphere size, solvent, solvent proportion, and SDS concentration can be studied to further optimize both self-assembly and deposition steps.

The monolayer self-assembly can be attained due to the use of anionic surfactants, in this case, sodium dodecyl sulfate [7,8]. Anionic surfactants are mostly skin and eye irritating, however, the use of very low concentrations should not be a problem. The development of a simple, low-cost approach is guaranteed with the Langmuir-Blodgett trough method optimization, as the most significant barrier for light-trapping schemes is its usual incompatibility with photovoltaic process technology for mass production.

Concerning the monolayer deposition and substrate transfer, as the size range is quite small, one should consider the fine-tuning of surface tension, as well as dipper and barrier moving rates, helping isolated nanosphere beads to merge and form a stronger, excellent film that does not deteriorate when transferring to the substrate.



# Chapter I: Introduction

## 1.1. Photovoltaic light-trapping technologies

Improving the quality of life worldwide creates an exponentially increasing need for energy. Highly efficient renewable energy sources and storage devices are needed to deal with such expensive demands. Considering the depleting fossil fuel stock and the devastating effects of global warming, photovoltaic (PV) technologies become one of the leading contenders in this field, as it offers a broad diversity of devices – each with their potential use and functionality [9–12]. Reports by SolarPower group (2020) [13] have also shown that the solar energy industry has a yearly net power generating added capacity as close as half of the total along with other sources.

Thin-film PV devices enable fast and cheap production methods, such as flexible roll-to-roll processes [14–16]. Moreover, these thin devices also benefit from lower material usage and thence further cost reduction. These are crucial factors at the industrial level for efficient production, making the technology attractive for application in affordable solar-powered consumer products such as mobile electronics (e.g. wearable PV), intelligent packaging (e.g. smart labels), IoT, and portable medical diagnostic services [2,3,17–21]. Thickness reduction also increases open-circuit voltages (and consequently efficiencies) due to lower bulk recombination.

The solar cells' efficiency is inherently limited by the absorber material's bandgap, as it sets the lower energy limit for absorption [22]. Nevertheless, thin-film PV suffers from additional absorption losses from the smaller travel path of light within the thin absorber film [23]. To overcome the second drawback, advanced light-management techniques must be used to improve the device's optical response. Among these, light-trapping (LT) architectures that create challenging conditions for light to escape the device have been the topic of many studies [1,24,33–37,25–32]. To improve PV devices' performance, one must adjust the thickness of the light-harvesting and charge-transporting layers. The development of new active materials and photonic structures, implemented via nano-patterning methods [38,39], has been key to improving overall performance, such as extending the absorption onset to the red region of the solar spectrum [40].

Soft-lithography techniques have since been employed, such as colloidal lithography (CL), as it that can be adapted to precisely nano/micro-pattern any material with the dimensions appropriate for efficient LT and implemented in any type of solar cell with different absorbers [31]. S. Haque *et al.* (2019) [4] has brought the concept of photonic LT structures to the emergent and highly promising class of perovskite solar cells (PSC's). For that, an inverted (substrate-type) PSC architecture with wave-optical structures is considered to allow the integration of the LT structures as a post-process on the cells' front contact. With the front-located wavelength-sized LT structures, higher PSC improvements were envisaged, avoiding

increasing the absorber layer roughness, thence avoiding electrical losses due to increased recombination. In particular, the optimized titanium dioxide ( $\text{TiO}_2$ ) void arrays, which were shown to be optically favorable when compared with the domes, enable photocurrent enhancements of over 21 % in PSCs with 250 and 500 nm perovskite layer thicknesses. On the other hand, M. Alexandre *et al.* (2019) [30] also presented an interesting conceptual approach to exploit UV energy in photonic-enhanced PSCs via the combined effects of LT and luminescent down-shifting (LDS). Subsequent research by Sanchez-Sobrado *et al.* [31,39,41] has revealed outstanding results of thin-film solar cells enhanced with photonic front structures that were patterned via LB. Using this CL method, highly uniform  $\text{TiO}_2$  nanostructures were attained via the production of LB-deposited colloidal masks (Figure 1.1.1).

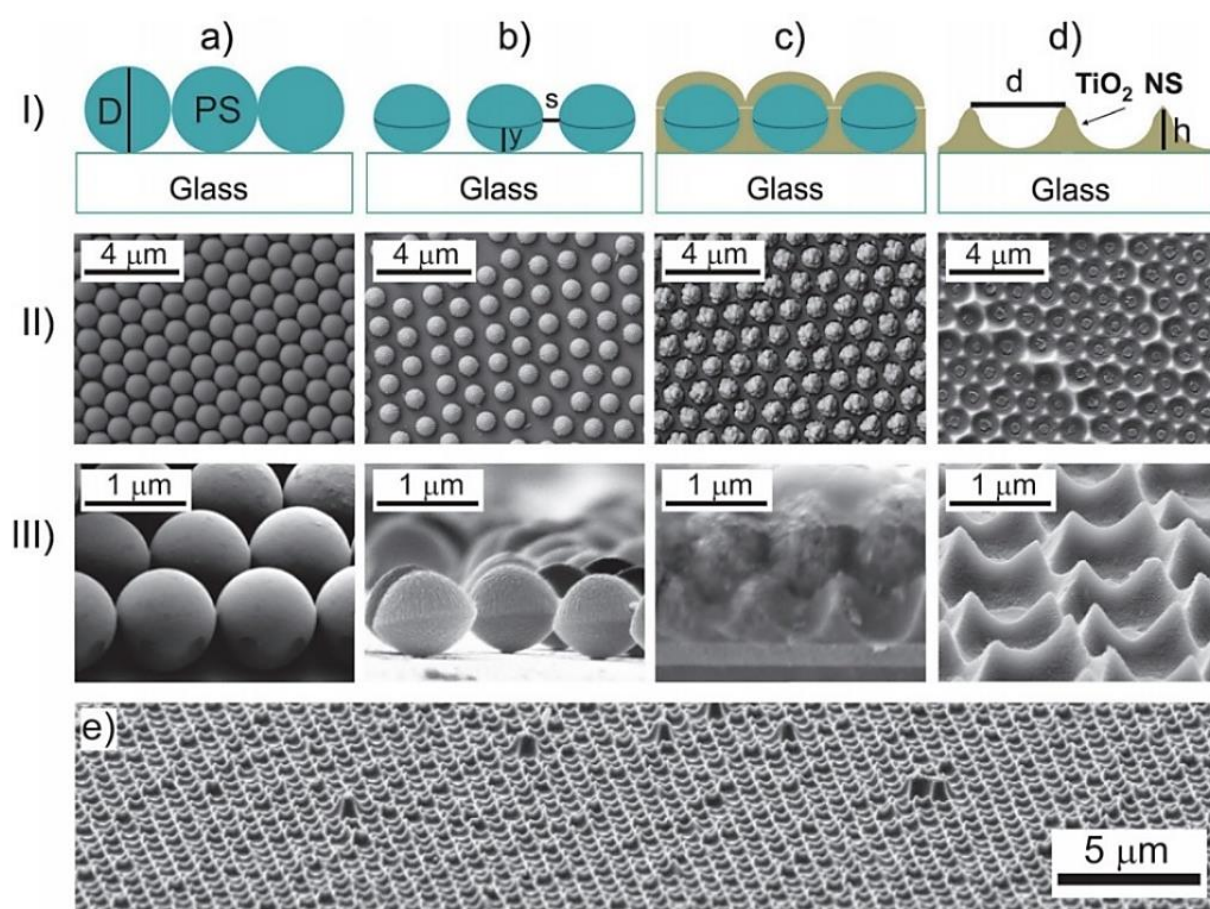


Figure 1.1.1 - Schematic drawings and SEM pictures of the samples obtained after the different steps of the  $\text{TiO}_2$  nanostructure construction via CL: (a) a hexagonal array of colloidal PS spheres is patterned on the cell front, (b)  $\text{O}_2$  dry etching, (c)  $\text{TiO}_2$  is deposited, filling the inter-particle spaces, (d) spheres are removed leaving an array of semi-spheroidal void-like features. The final  $\text{TiO}_2$  structure, (e) uniformly covers the entire sample area. [39]

## 1.2. Colloidal lithography approach

Colloidal lithography (CL) [1,4] is presently considered the most promising nano/micro-structuring method for photonic and PV applications [31]. It is an especially interesting approach since it can pattern any material and is not affected by common limitations of nanoimprinting lithography or photolithography. It consists of four main stages (see Figure 1.1.1): the colloidal deposition, the patterning mask production via RIE, the deposition of the patterning materials (such as TiO<sub>2</sub> [39,41], AZO [1] or IZO [31,41]), followed by the final nano/micro-structure production after colloidal lift-off [1]. This shows the high versatility of this method for implementation in various applications. The most synthesized particle materials for use in CL are polystyrene (PS), polymethyl methacrylate (PMMA), and silica. The choosing of the preferred sphere surface chemistry depends on the desired application. [42,43]

### 1.2.1. Colloidal self-assembly and monolayer formation

The self-assembly of colloidal particles, which is believed to be a key technology for next-generation surface and volume nanostructuring applications [44–48], is a process in which colloidal particles spontaneously arrange into ordered superstructures (Figure 1.2.1) [49]. Based on the type of dominant force driving the self-assembly, these methods can be organized into four classes: physical (process dominated by shear forces, adhesion, and surface structuring), fluidic (by capillary forces, evaporation, surface tension), external fields (by electric and magnetic fields) and chemical (by chemical interaction, changing the surface charge or creating binding sites) [49,50].

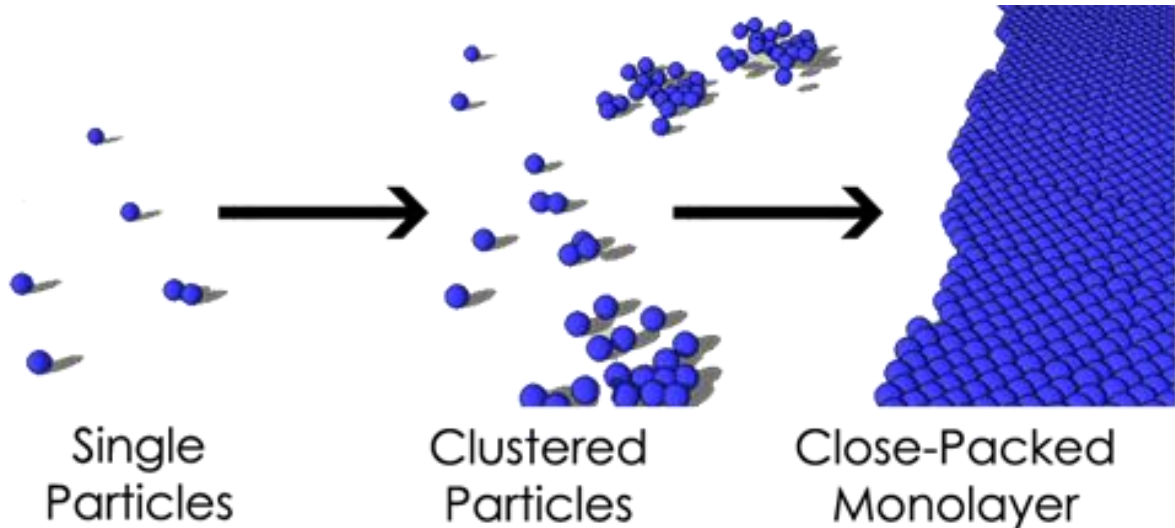


*Figure 1.2.1 – 3D illustration of the self-assembly of colloidal particle structures forming a hexagonal close-packed array (also known as honeycomb), which results in the highest in-plane packing density – single particles tend to bond with others due to either physical, fluidic, external fields, or chemical force driving, from single, to small clusters to larger monolayers.*

### 1.2.2. Substrate deposition of colloidal monolayers

Three techniques should be emphasized when transferring the monolayer to the desired substrate (see Figure 1.1.1a). The spin coating technique (Figure 1.2.2a) can be considered a simple process for rapidly depositing thin coatings onto relatively flat substrates [66–69]. The doctor blade technique (Figure 1.2.2b) is also simple, and highly-scalable, however, it is quite difficult to attain a purely 2D thin-film [51]. However, the resulting thin-films tend to be less uniform than those produced by dip-coating methods like Langmuir-Blodgett, in which the formation of a monolayer is more accurately assured yet simple to scale to industrial levels. [52]

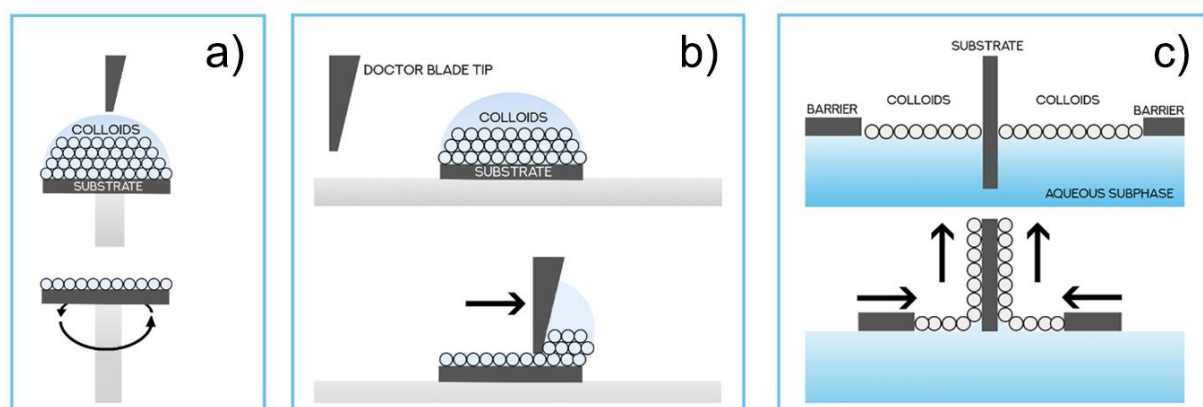


Figure 1.2.2 - Production of a colloidal monolayer using (a) a spin coating technique, (b) Doctor Blade trough, (c), and a Langmuir-Blodgett trough.

Langmuir-Blodgett [53], as described by Figure 1.2.2c, is a simple, low-temperature method in which colloidal monolayers [54] can be deposited onto substrates by producing a floating monolayer film at the air-water interface (Langmuir-film) and then transferring it onto a solid substrate [55]. At first, the amphiphilic colloidal particles are dispersed in a volatile water-immiscible solvent (ethanol, diacetone, chloroform, benzene, among others [56,57]) to prepare the colloidal solution. Then, small amounts of the solution are carefully deposited and spread onto the air-water interface at the LB trough using, for instance, a microsyringe. Afterward, the colloidal particles spread throughout the interface on the trough, and the volatile solvent evaporates, leaving a colloid monolayer at the interface [58]. Finally, the immersed substrate is withdrawn vertically from the aqueous subphase while the lateral barriers close in towards the substrate, at controlled rates, thereby transferring the colloids stabilized at the air/water interface to the upwards moving substrate [53], resulting in a successfully deposited monolayer colloidal film [6].

The fabrication of monolayers by interface coating methods as LB has been subject to numerous studies, varying the colloids' size, the solution amount and proportion, temperature, deposition angle, and others [8,24,59]. Surface and interface chemistry is of paramount

importance for defining how smaller particles float and get packed [8,38,60]. For instance, smaller particles (under 1  $\mu\text{m}$ ) tend to sink into the aqueous subphase, contrasting with larger ones that typically float [1,7,8,31]. It is believed that the use of surfactants in the aqueous subphase may enhance the floating and film production of colloidal particles at the air/water interface, with larger areas and mechanical strength [7,8,60]. Surfactant molecules tend to occupy the media interfaces and join the incoming colloidal particles together, thus opposing their dispersion caused by the Brownian motion (Figure 1.2.3). The surface assembly forces tend to enlarge the array area, increasing the monolayer order and coverage [59,61]. There is also a reduction of surface tension at the interface due to the presence of the surfactant, which favors colloidal particle movement along the interface to find their lowest energy configuration, resulting in an optimally-ordered hexagonal close-packed monolayer [62]. Adding a surfactant, however, may introduce undesired contamination to the interface [7,63].

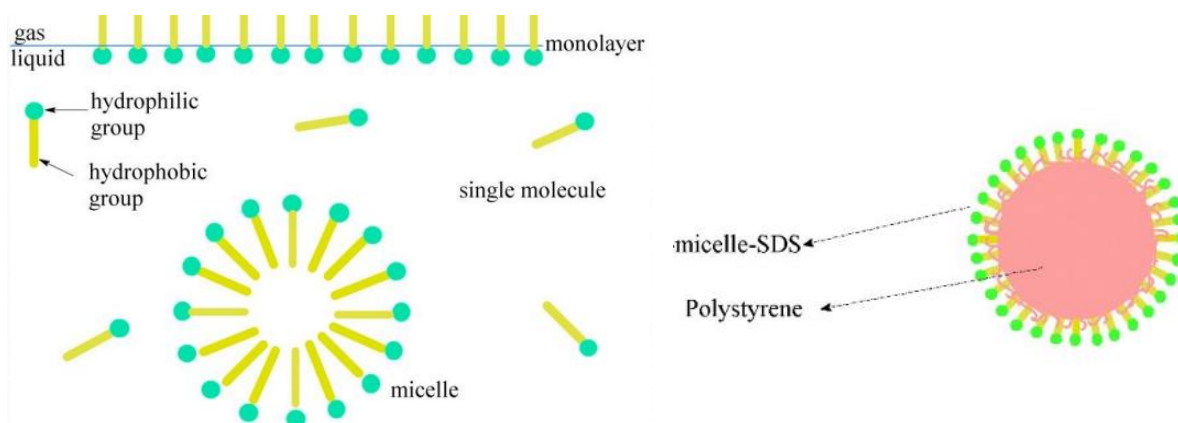


Figure 1.2.3 - Schematic of surfactant molecules and PS micelles in aqueous solution [61]

Vogel *et al.* (2011) [8] described that small amounts of SDS at the interface influence capillary forces and form a soft barrier that facilitates the crystallization process. Furthermore, when carboxylic acid-functionalized colloids were used for the monolayer crystallization, an increase in the pH of the subphase was found to increase the order in the resulting monolayer. The author also increased the aqueous sub-phase pH to 11, which improved the monolayer quality. On the other hand, Ye *et al.* (2017) [7] introduced a simple approach to produce high-quality hexagonally ordered arrays of polystyrene (PS) microspheres via an air-water self-assembly method, in which SDS was added to the self-assembly aqueous subphase to change the water surface tension.



## Chapter II: Experimental

The production of nanosphere-coated substrates followed a procedure in which the monolayer self-assembly and its transfer to the substrate were studied sequentially. The full production technique is described in this section. Steps 2.3 and 2.4 were previously simulated in Petri dishes to allow the further LB deposition of the best self-assembly films. Short, numbered videos were recorded to illustrate some of the key aspects of the method below and included in the following Google Drive URL: <https://bit.ly/3ob1Jlo>.

### 2.1. Langmuir-Blodgett trough

For the LB method, introduced in Section 1.1.2, we used the KSV NIMA LB equipment. Based on the approach of Ariga *et al.* (2013) [6], the barriers and the trough were well clean with ethanol and deionized water. Then, we carefully filled the trough with 750 ml of deionized water. Two substrates were stuck together back-to-back and lowered diagonally. When lowering, the dipper zero was set right before contact between the substrates and the air-water interface. The barriers were then closed at their maximum, where the barrier zero was set.

### 2.2. Substrate preparation

A4 sheets of PET, with ITO deposited onto one of its faces, were cut into square substrates of 2.5 cm × 2.5 cm, then rubbed with detergent and dipped in acetone, IPA, and deionized water for 10 minutes using a sonication bath. The substrates were dried using a flow of compressed nitrogen and then subjected to exposition to UV-Ozone for 15 minutes for wetting enhancement.

### 2.3. Aqueous sub-phase preparation

Inspired by methods developed by Vogel *et al.* (2011) [8] and Ye *et al.* (2017) [7], 3.5 mg of SDS were carefully added using a lab spatula, and spread in the aqueous subphase, to attain variable concentrations of 4.5 mg/l, respectively. The surface tension was calibrated to be less than 0,8 mN/m and the barriers were slowly open at the lowest manual speed (10%) till the maximum opening distance. Using a microsyringe, 1 ml volume of ethanol was added to the whole water surface to facilitate further colloidal dispersion.

### 2.4. PS nanospheres preparation

Firstly, a commercial nanosphere aqueous solution (microParticles GmBH PS-R-0.6, 5 wt%) was agitated for 60 seconds in an MS-X Vortex Mixer. Using a micropipette, a nanospheres volume of 200 µl was firstly cast onto an Eppendorf, with a non-polar solvent (either pure ethanol - EtOH 95.0% - diacetone, or chloroform). This proportion was defined as 1:3. Finally, the solution is again submitted to 60 seconds in the MS-X Vortex Mixer.

## 2.5. PS nanospheres deposition

Using a microsyringe, the PS-ethanol solution was carefully and slowly cast to the air-water interface, guaranteeing the best possible interfacial spreading (see video: <https://bit.ly/3af35rX>). To join separated grains, the barriers were set to be closing at a certain rate till a target surface tension (threshold) was met (video: <https://bit.ly/2K5lWuy>). The closing rate was chosen to be fast at first (50 mm/min for a starting 40% progress) to avoid fast solvent evaporation from single beads, which would prevent their desired merge. The speed would then be reduced up to 10 mm/min until a high-quality and colorful thin film was observed (video: <https://bit.ly/34aGau1>). When that condition was met, the target threshold was set to 0 to initiate both the dipper raise and barrier closing at a fixed rate of 2 mm/min, fully transferring the forming monolayer to the substrates (video: <https://bit.ly/34cIcd3>).

## 2.6. Characterization - SEM and ImageJ

Surface morphology analysis was performed while using the SEM Hitachi T3030 Plus Tabletop equipment, available at CENIMAT|i3N, at a constant accelerating voltage of 15 kV. Magnifications in the range of 1000x-8000x were used to produce the resulting SEM images. To compare contrasting samples, the same contrast and brightness conditions were applied.

Recurring to the same SEM imagery, one was able to evaluate the quality of the close-packing of the nanosphere structure and the substrate area coverage (SAC) by using the Image Threshold, Fast-Fourier Transform (FFT), and Radial Profile analysis tools and plugins of the *ImageJ* software, according to work by several authors [65-60,72]. Both the software and the plugins were downloaded from its official website (<https://imagej.nih.gov/ij/download.html>).

Performing an Image Threshold selects the brighter pixel areas (which show the deposited nanospheres domains) and reflects its total SAC [64-66]. On the other hand, the FFT function consists of the graphical representation of the previous grayscale image in the frequency domain, thus displaying the structure ordering. As far as the Radial Profile plugin is concerned, it produces a profile plot of normalized integrated intensities around concentric circles as a function of distance. In this work, the distance was presented as a factor of the minimum distance between close-packed spheres (which is equal to the sphere diameter) to compare to the values suggested further in Figure 3.2.

More information on the ImageJ characterization can be found in Appendix A, as a simpler method was developed to only use ImageJ throughout the whole analysis.

## Chapter III: Results and Discussion

This chapter intends to discuss the optimization of the different parameters that were studied to improve the colloidal monolayer quality, such as the polystyrene (PS) nanospheres sizes, the solvent and its proportion in the colloidal solution, and the sodium dodecyl sulfate (SDS) concentration in the Langmuir-Blodgett (LB) aqueous sub-phase. The quality of the self-assembly was evaluated by the exhibition of a uniform colorful refraction pattern at the air-water interface (mostly via a petri dish simulation of the LB trough). As far as the LB deposition is concerned, a good substrate coverage is desired, while it is also expected to achieve excellent area-uniform close-packed honeycomb structures, inspected by scanning electron microscopy (SEM) and ImageJ tools – Image Threshold, Fast Fourier Transform (FFT) and Radial Profile.

The Image Threshold allows for the extraction of the surface area coverage (SAC) of each deposition. Its maximum value ( $SAC_{MAX}$ ) can be calculated following the relation between the area occupied by perfectly close-packed spheres and the total available area (Figure 3.1).

$$SAC_{MAX} (\%) = \frac{1 + 6/3 \text{ Circle Area}}{1 \text{ Hexagon Area}} = \frac{3(\pi * r^2)}{\frac{3(2r)^2\sqrt{3}}{2}} = \frac{\pi}{2\sqrt{3}} \sim 90.7\%$$

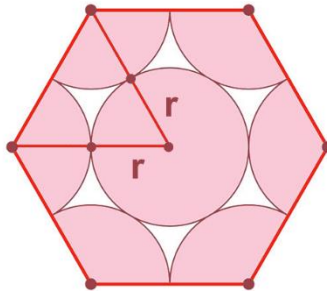


*Figure 3.1 - Close-packing hexagonal geometry and the relation between the sphere size and the corresponding honeycomb structure with surrounding particles.*

Here we define the Area Coverage Success ( $ACS = SAC_{EXP}/SAC_{MAX}$ ) as the ratio between the experimental SAC value, obtained for each deposition with Image Threshold, and the theoretical maximum SAC value of 90.7%.

By applying the Fast Fourier Transform (FFT) to the scanning electron microscopy (SEM) images for each batch of samples, it was possible to perceive the long-range ordering and its quality. The FFT function consists of the graphical representation of the previous grayscale image in the frequency domain in respect of its structure ordering, allowing for the numerical representation of contrasting FFT images. This tool establishes a relation between a central particle and its surroundings, as in a perfect close-packed structure we would follow a model pattern of distances (depicted in Figure 3.2). An ordered array should show bright and

clear peaks positioned within a hexagonal shape, coinciding with the surrounding particles centroids, while an unordered array would be represented by fading concentric circles or rings [66–69]. On the other hand, a good FFT peak definition can also be related to how much the array resembles a honeycomb structure. The FFT imagery also provides crucial information regarding directional structure ordering. Pixel intensities were summed along a radius from the center to the edge of the image to quantify the relative contribution of objects oriented in that direction. The number of rings (FFT-R) relates to the uniformity throughout the analyzed area – it can be defined as the number of reasonably focused concentric circles in the FFT image. The larger the value of FFT-R, the better the periodicity among the total area [69].

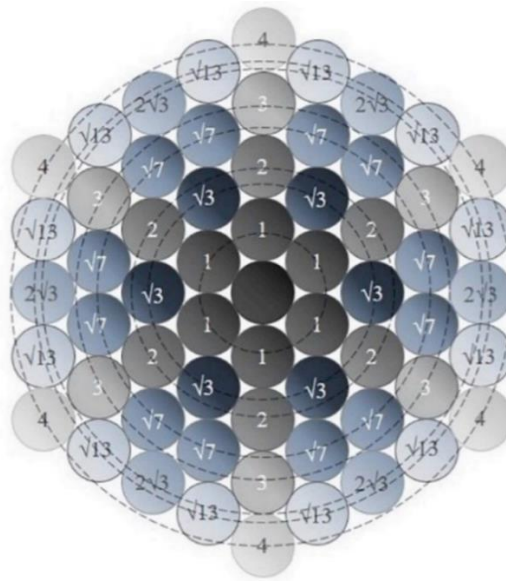


*Figure 3.2 - Schematic diagram showing an arrangement of perfect hexagonally close-packed colloidal monolayer structure. The numbers inside each circle indicate its distance from the central sphere (between centroids). [70]*

To quantitatively analyze the quality of particle arrangement, we used the radial distribution function (Radial Profile), which is a mathematical function that gives the probability of finding a particle at a certain distance from a reference particle [70]. This function has been used to describe the characteristic of the lattice structure in solids through the positions, separations, and heights of the distinct sharp peaks. It consists of plotting the angle integrated FFT as a function of the distance (radius) to a central point in the image. Such analysis transforms the 2D FFT into a 1D function with a single variable, thus assisting in the assessment of the resulting order and deposition quality. To prevent any effects that magnification and sphere size variation may have in further radial profile comparisons, an additional step was employed: the normalized integrated intensity was defined as a function of distance (as a factor of the sphere diameter). The schematic displayed in Figure 3.2 shows the fraction of the diameter that represents the distances between the centroids of close-packed particles. The resulting plot of a perfect arrangement shows multiple peaks at the distances 1,

$\sqrt{3}$ , 2,  $\sqrt{7}$ , 3,  $2\sqrt{3}$ ,  $\sqrt{13}$ , 4 times the distance between close-packed spheres centroids [69]. Also, the more, intense, distinct, and narrower Radial Profile peaks, the better arrangement, as it indicates that the expected intersphere distances are fulfilled along the analyzed area [71].

### 3.1. PS nanospheres deposition (1.3 $\mu\text{m}$ size)

Polystyrene nanospheres have been shown to typically float when deposited onto the air-water interface, however sinking effects are observed when depositing smaller spheres. A simple, conventional LB method [39] was used to deposit a honeycomb array of 1.3  $\mu\text{m}$  diameter polystyrene nanospheres in flexible substrates. Self-assembly occurred naturally at contact with the air-water interface, and a fully deposited substrate was achieved.

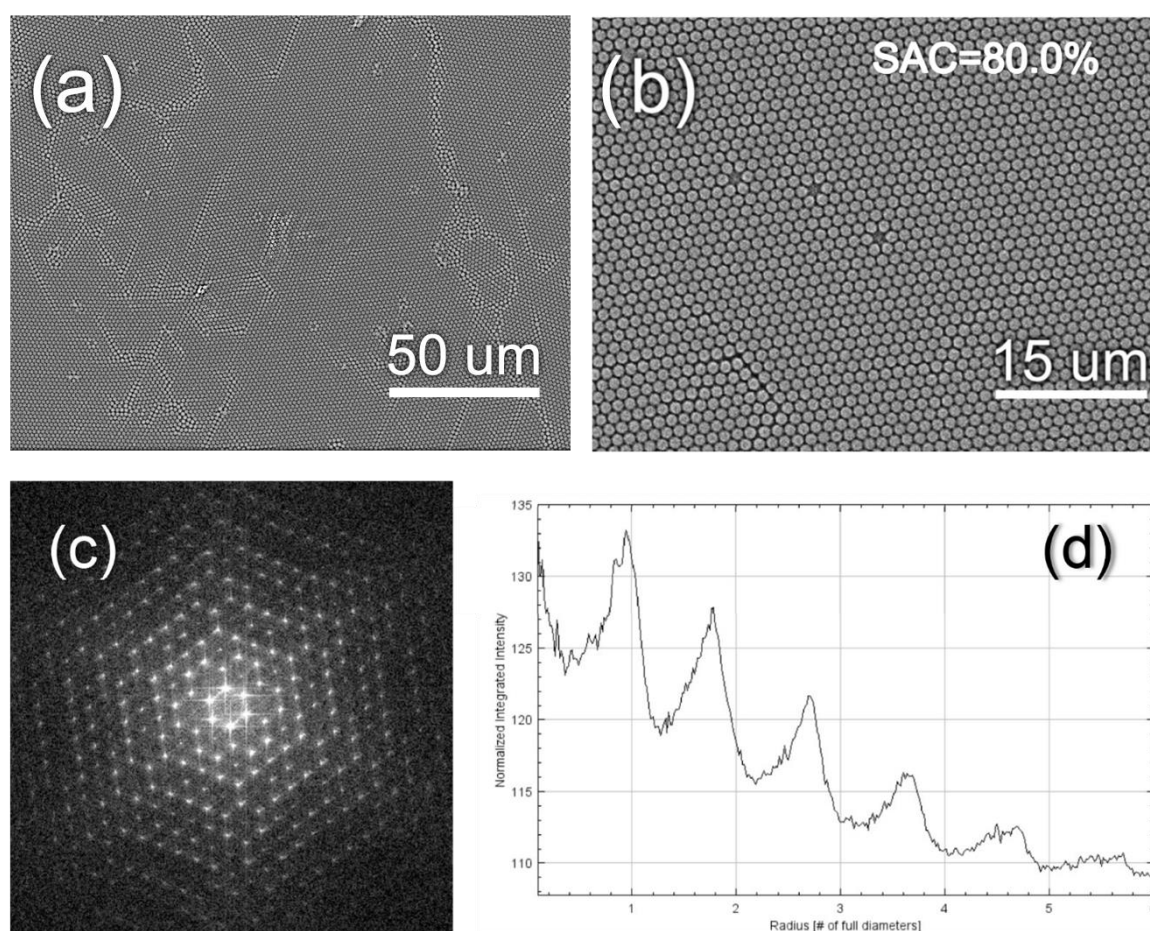


Figure 3.1.1 – (a,b) SEM images of the deposition of 1.3  $\mu\text{m}$  PS nanospheres in PET-ITO using a conventional LB method; (c) Fast Fourier Transform of SEM image b (d) Radial profile plot of the FFT image: normalized integrated intensity as a function of distance (the number of spheres diameters)

After contrast increase and threshold definition, the ImageJ analysis resulted in a SAC of 80%, which should translate, according to the maximum value of 90.7% calculated in this chapter's introduction, to an ACS of 88.2%. The FFT image (Figure 3.1.1c) shows several well-

defined peaks, which is a sign of being in the presence of a periodic structure [69]. A total of 6 contrasting rings are suggested by both Figure 3.1.1c and the plot in Figure 3.1.1d, with 6 peaks – the larger the number of rings, the better the periodicity among the total area [69]. Multiple radial profile peaks were clearly seen at approximately identical positions (Figure 3.1.1d) as expected in Figure 3.2, indicating a good arrangement quality. However, as it is possible to witness in the FFT image, the  $\pi/3$  direction peaks lose definition as the distances grow larger. Good overall periodicity and close packing were achieved within these structures, with very small directional disordering. For 1.3  $\mu\text{m}$  nanospheres, in similarity with larger ones, it was perceived that a conventional LB method was naturally capable of resulting in high-quality arrays. This experiment was intended to better understand the results that one should aim for when producing state-of-art nanospheres arrays using smaller sizes, this work’s main goal.

### **3.2. PS nanospheres self-assembly (below 1 $\mu\text{m}$ size)**

Although the deposition of PS sizes of 1.3  $\mu\text{m}$  is well-succeeded within conventional Langmuir-Blodgett self-assembly and substrate dipping methods, its use with smaller colloid sizes did not manage to provide reasonable results. According to the simulation studies performed by the PV research team of CEMOP and CENIMAT [29,30], the preferential dimensions of the CL patterns should be within the 0.5-1  $\mu\text{m}$  range for the thin-film solar cell technologies analyzed (namely based in silicon, perovskite, or CIGS PV materials). On the other hand, the team’s experimental results also showed that a high-quality deposition with smaller PS nanospheres (below 1.3  $\mu\text{m}$ ) would be especially challenging since the conventional method would not provide for their spontaneous floatation for the monolayer self-assembly in Langmuir-Blodgett. Therefore, this was a key issue addressed in this thesis, aiming for the controlled deposition of PS sphere arrays with sizes in the preferential 0.5-1  $\mu\text{m}$  range. After guaranteeing the floatation of these smaller nanospheres, optimizing the production of a high-quality film and its deposition onto flexible substrates would be key for a good performance.

#### **3.2.1. Preliminary PS nanospheres self-assembly experiments**

At first, the conventional self-assembly approach described in the previous section was reproduced in Petri dishes to study the spontaneous self-assembly of 0.5 and 0.6  $\mu\text{m}$  nanospheres. However, no nanosphere floatation could be found in the presence of the proposed 1:3 ethanol colloidal solvent, as the simulated aqueous subphase would become turbid and therefore one could conclude the nanospheres had sunk (Figure 3.2.1).

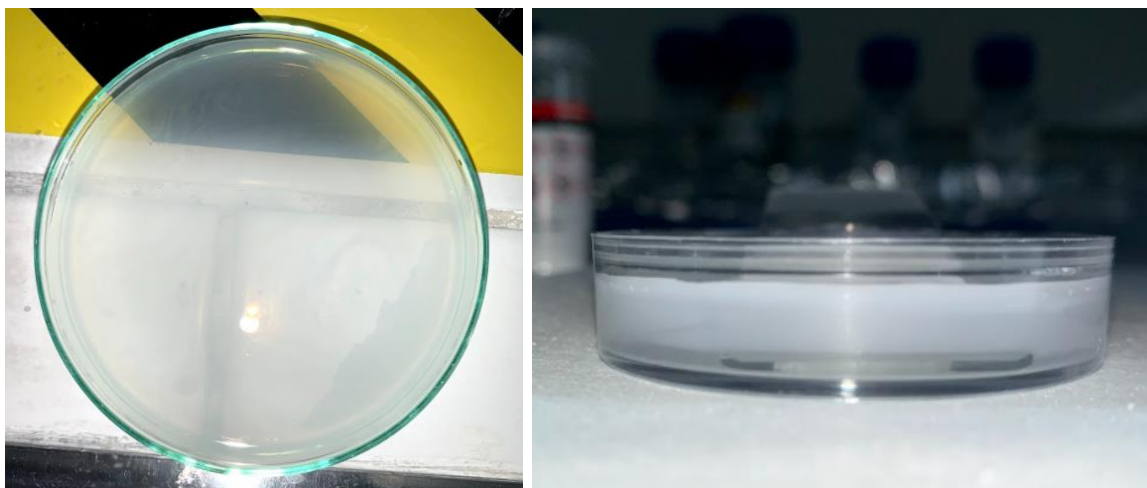


*Figure 3.2.1 – Top (left) and side-view (right) of a turbid self-assembly aqueous subphase, a condition observed for both 0.5 and 0.6  $\mu\text{m}$  PS nanospheres - a sign of sinking colloidal particles and absence of interfacial monolayer formation*

This same outcome was reported for both 0.5 and 0.6  $\mu\text{m}$  nanosphere sizes. Although further testing was performed by varying the solvent (ethanol, diacetone, chloroform, among several others) and the PS-solvent proportion (1:2, 1:3, and 1:4), better results could not be achieved. It was not possible to detect a colorful film forming at the interface, as suggested in the Materials and Methods chapter. The inclusion of a centrifugation step, in which the initial nanosphere aqueous solution would be dried off in four centrifugation cycles, showed small improvements in the self-assembly - by fixing a 1:3 proportion of either ethanol or diacetone, one could witness the forming of very weak interfacial film, that would sink rapidly.

### **3.2.2. Surfactant addition on the self-assembly aqueous subphase**

Following the premise that the use of surfactants, such as SDS, in the self-assembly aqueous subphase would prevent sinking effects [7,8], small amounts (4,5 mg/l) of SDS were dissolved before the nanosphere microsyringe dropping onto a sliding glass, to prevent heavy drops. A PS-ethanol proportion of 1:3 was fixed in this experiment. In any of the tested concentrations of 3 mg/l, 4.5 mg/l, and 6 mg/l and nanosphere sizes of 0.5 and 0.6  $\mu\text{m}$ , the addition of SDS showed significant improvement in the spontaneous nanosphere floatation and self-assembly, with small sinking loss when compared to conventional LB methods (Figure 3.2.2).

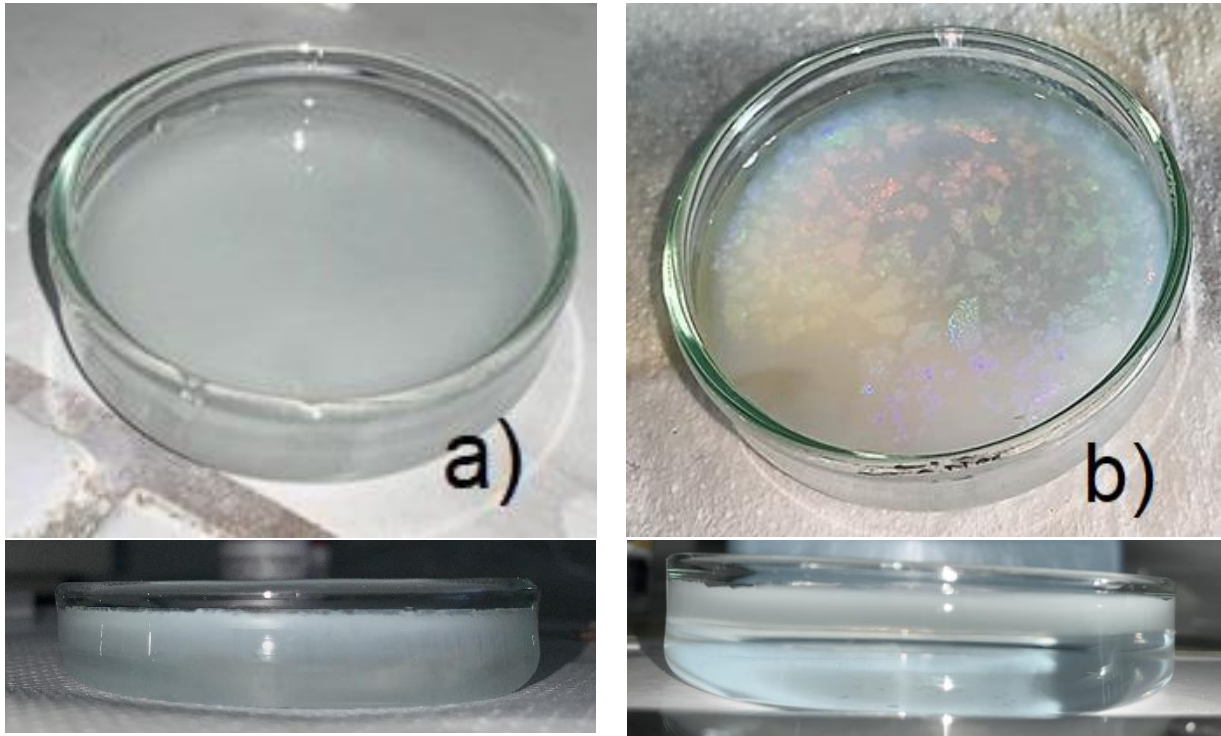


Figure 3.2.2 – Top and side views on the (a) floatation and self-assembly study for petri dish simulations on the deposition of  $0.6 \mu\text{m}$  PS nanospheres on aqueous subphase without adding SDS and (b) adding a small concentration of SDS ( $4.5 \text{ mg/l}$ ). Turbid subphase and colloidal precipitation were observed within the conventional method, while the addition of a small amount of SDS developed bright colorful interfacial clusters, well defined in thickness and surface.

However, sinking effects would be fastened and highly induced by reducing or increasing the SDS concentration. As reported in the Introduction chapter and depicted in Figure 1.2.3, the use of surfactants in a gas-liquid interface creates a surfactant thin layer with the hydrophilic tail towards the water and the hydrophobic tail towards the air. In this case, when contacting with the interface, the non-polar solvent dissolved polystyrene spheres would spread on top of this layer easily. The excessive concentration of SDS would induce the formation of micelles, which would bring the nanospheres clusters into sinking – which could be seen in both top and side views of the petri dish after some resting minutes. On the other hand, using a smaller concentration would tend for a lacking floatation effect, as seen in the previous section. It is also natural to observe the formation of isolated nanosphere clusters, as this is a simulation of the LB trough and therefore it lacks the barrier closing effect on its merging.

NaCl was also tested as a sub-phase specimen, as proposed in a work by Moon *et al.* (2011) [72], in which the concentration of  $10 \text{ g/l}$  was used hoping to attain decent floating and self-assembly properties. Within this work, average, and border concentrations of  $5 \text{ g/l}$ ,  $10 \text{ g/l}$ , and  $100 \text{ g/l}$  were studied, however, none would provide any sort of floatation enhancing effect and all particles sunk.

### 3.2.3. Nanosphere/solvent proportion variation

In this next set of experiments, the mixture of the original commercial nanosphere solution and the main solvent was tested to be 2:1, 1:1, 1:2, 1:3, and 1:4 (Figure 3.2.3 and Google Drive: <https://bit.ly/3mi0Kyw>). In this experiment, fixed conditions were a 4,5 mg/l concentration of SDS (sodium dodecyl sulfate), ethanol as a solvent, and 0.6  $\mu\text{m}$  PS nanospheres.

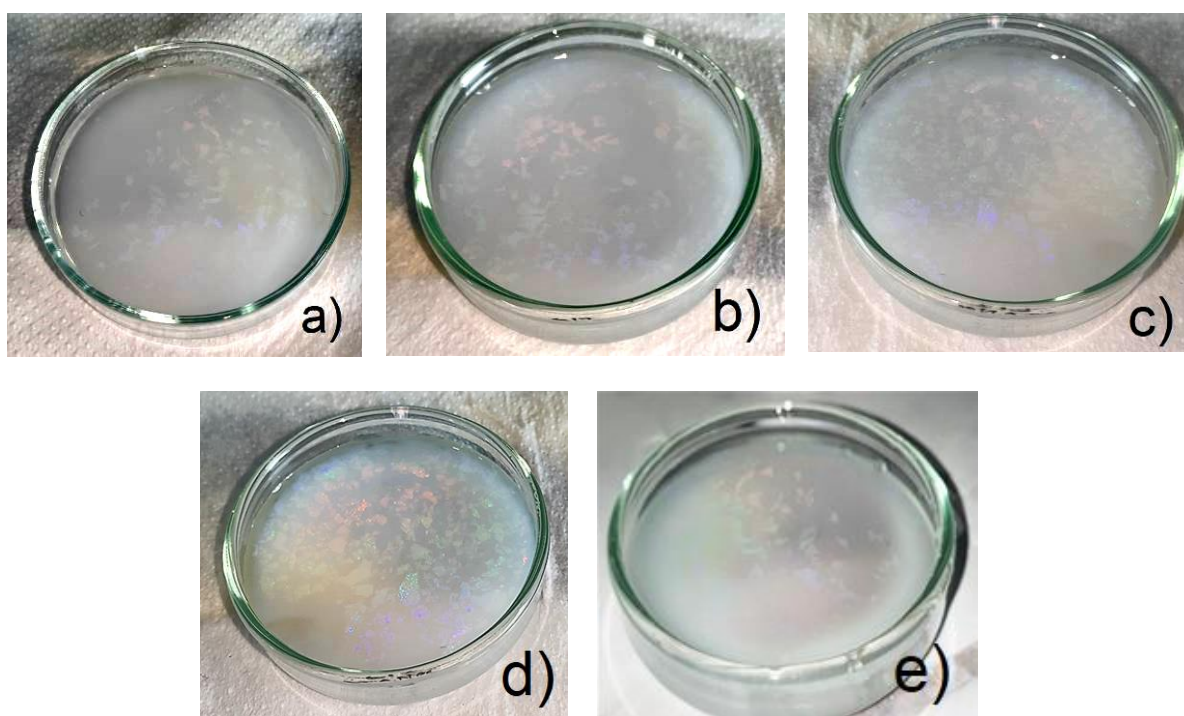


*Figure 3.2.3 - Petri dish simulation of five different PS:ethanol proportions with 0.6  $\mu\text{m}$  PS nanospheres: (a) 2:1; (b) 1:1; (c) 1:2; (d) 1:3; (e) 1:4*

As seen in Figure 3.2.3, there is a tendency among the first four proportions, which could mean that an increase in the solvent volume could improve the interfacial monolayer assembly. However, as noticed in Figure 3.2.3e, the excessive use of ethanol (solvent) fastens the degradation of the monolayer clusters, mainly due to the strong interaction between ethanol and SDS. In reasonable smaller volumes, ethanol slows down the degradation reaction and hence contributes to a long-lasting self-assembly monolayer. A 1:3 proportion was therefore kept as the most promising for further experiments.

Since the achieving of a spontaneous floatation and self-assembly of polystyrene nanospheres was our first main goal, we were then in conditions to proceed for its reproduction in the Langmuir-Blodgett trough. 0.5  $\mu\text{m}$  sized nanospheres were then discarded from further studies due to its lacking quantity and sizes up to 1.0  $\mu\text{m}$  still being optimal in light-trapping applications.

### 3.3. PS nanospheres deposition (below 1 $\mu\text{m}$ size)

#### 3.3.1. Size-variation effect on the PS nanospheres deposition

Different PS nanosphere diameters 0.6  $\mu\text{m}$ , 0.7  $\mu\text{m}$ , and 0.9  $\mu\text{m}$  were tested while fixing the best performing conditions at 1:3 proportion, ethanol as a solvent, and a sub-phase SDS concentration of 4.5 mg/l (Figure 3.3.1). These size variations did not seem to a significant effect on the monolayer self-assembly, as all three produced stable colorful films. Nevertheless, 0.9  $\mu\text{m}$  deposited substrates shown low substrate deposition, being discarded (Table 3.3.1).

Table 3.3.1 – Effect of the addition of SDS (4.5 mg/l) in the monolayer self-assembly and substrate deposition for each PS nanosphere diameter

PS Nanospheres Size ( $\mu\text{m}$ )	Self-Assembly Monolayer Quality	Substrate Deposition Coverage
0.6	Good	Decent
0.7	Good	Decent
0.9	Decent/Good	Bad

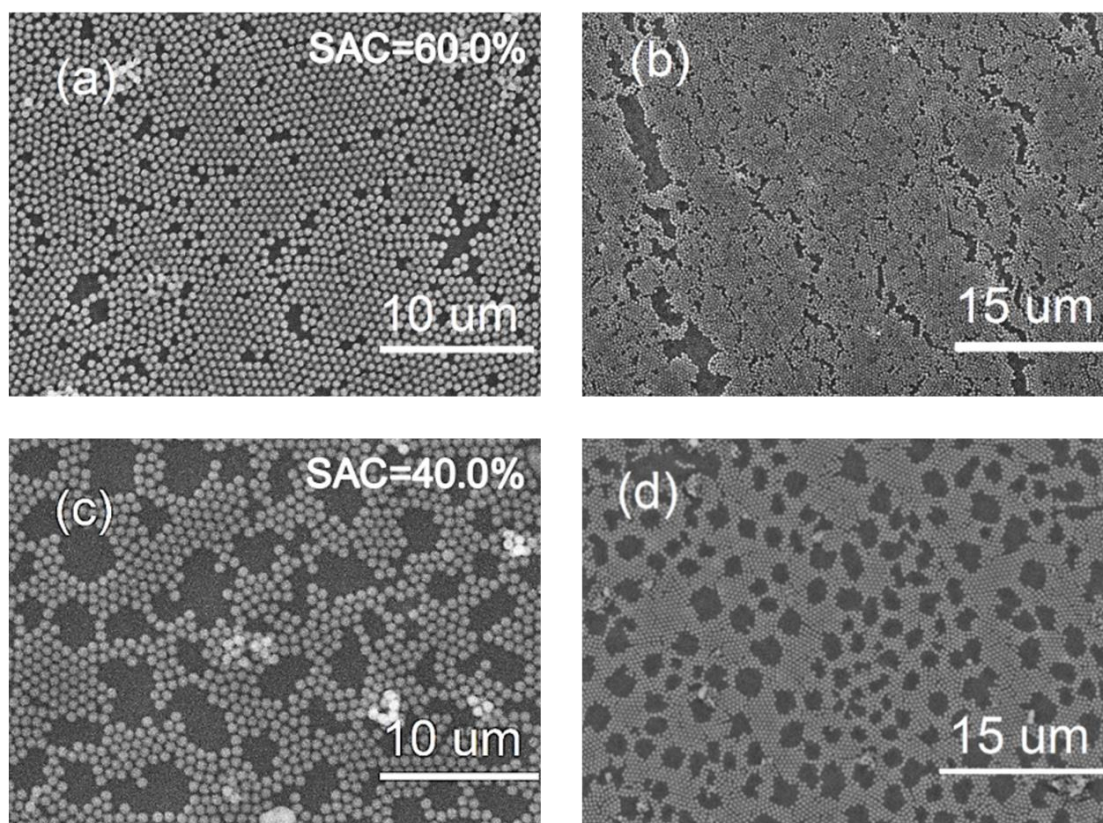


Figure 3.3.1 - SEM images of the PS nanosphere size variation effect: (a,b) for 0.6  $\mu\text{m}$ ; (c,d) for 0.7  $\mu\text{m}$ ;

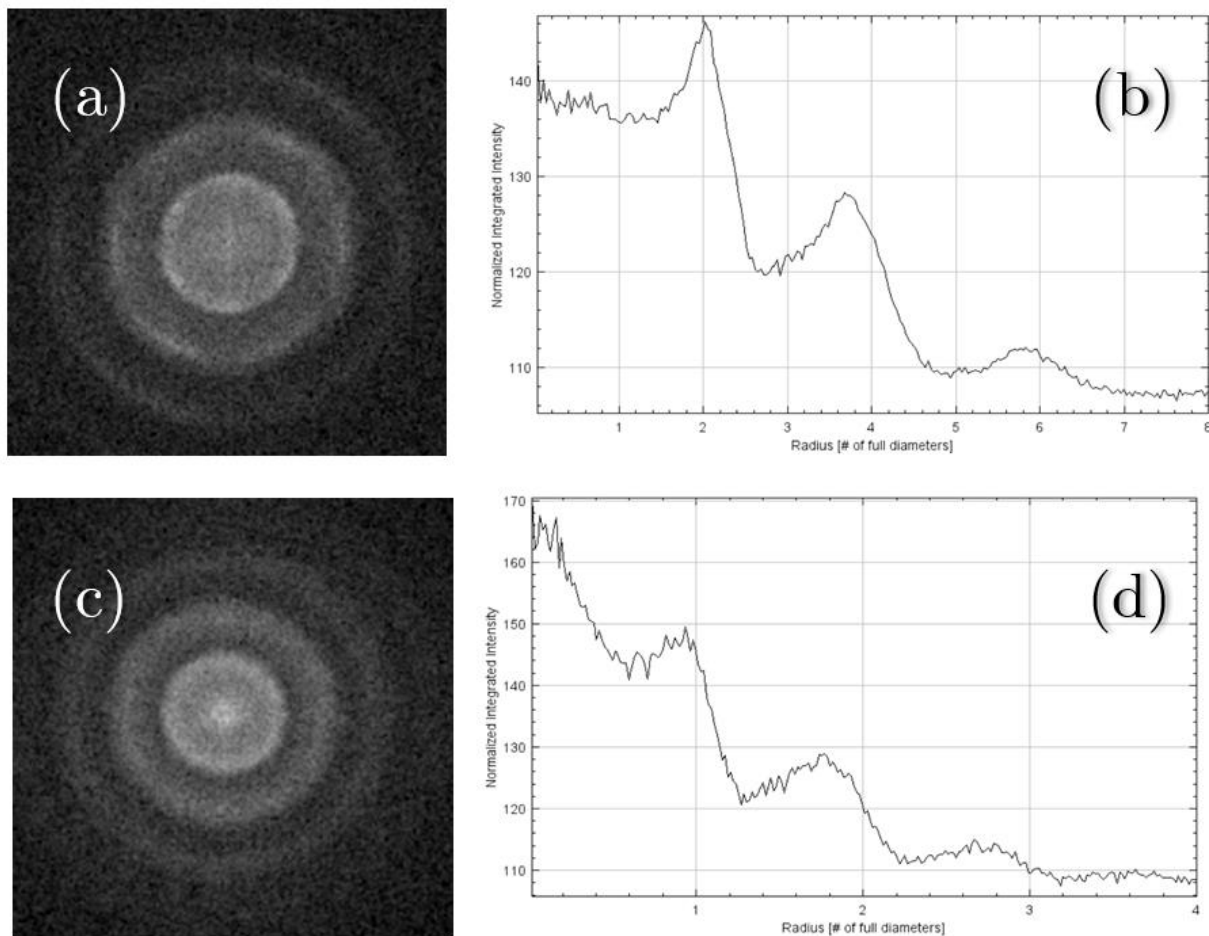


Figure 3.3.2 - Fast Fourier Transform of the SEM image and radial profile, respectively, for 0.6 (a,b) and 0.7  $\mu\text{m}$  (c,d) PS nanospheres.

The 0.6  $\mu\text{m}$  ImageJ analysis resulted in a SAC of 60%, which should translate to an ACS of 66.2% (Figure 3.3.1a). The FFT image (Figure 3.3.2a) shows low-definition hexagonal cycles, with no well-defined peaks being defined. The fact that the hexagonal dispersed FFT peaks can be seen is an indicator that some ordering can be found. The radial profile (Figure 3.3.2b) gives us the information that the average distances from the closest surrounding spheres are double than what should be expected, therefore, close packing was not totally achieved.

Concerning the 0.7  $\mu\text{m}$  sample, the ImageJ analysis resulted in a SAC of 40%, which should translate to a smaller ACS of 44.1% (Figure 3.3.1c). Well-defined peaks were also not found in the FFT image (Figure 3.3.2c), but the cycles seem to be more of a circular shape than for the 0.6  $\mu\text{m}$  samples, more hexagonal. The peaks in the radial profile plot (Figure 3.3.2d) give us the information that the average distances from the closest surrounding spheres are quite near to the expected values. However, with the peaks being small and wide, the intersphere distances do not seem to be uniform throughout the analyzed area.

These results indicate that this method tends to provide better results for 0.6  $\mu\text{m}$  spheres, while also not invalidating future studies for 0.7  $\mu\text{m}$ , which shows decent depositions.

### 3.3.2. Solvent-variation effect on the PS nanospheres deposition

As a solvent for the nanospheres solution, the use of either ethanol or diacetone showed similar quality of air-water monolayer formation for a fixed 1:3 proportion, which was revealed to be the best performing proportion for both solvents. The SEM results for each batch are reported in Figure 3.3.3.

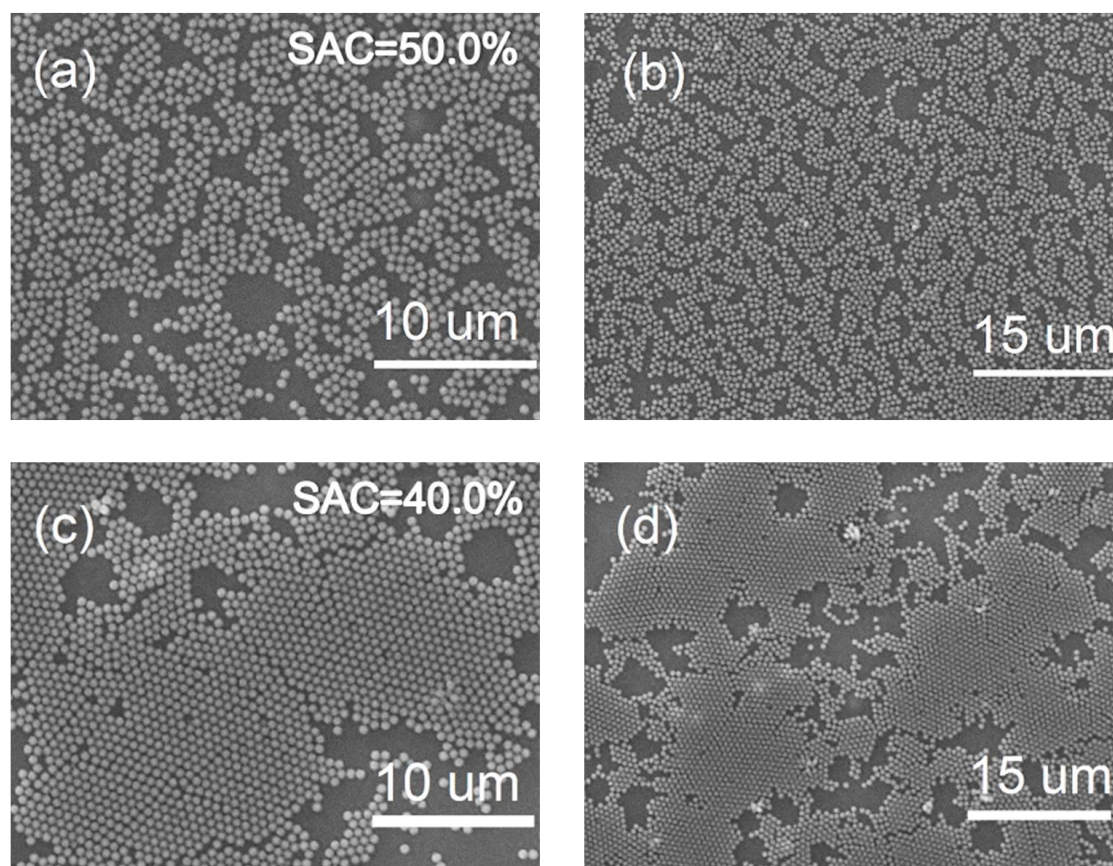


Figure 3.3.3 - SEM images of 0.6  $\mu\text{m}$  PS nanospheres depositions with different solvents: (a,b) ethanol; (c,d) diacetone

The ethanol sample ImageJ analysis resulted in a SAC of 50%, which should translate to an ACS of 55.1% (Figure 3.3.3a). Concerning the diacetone sample, the ImageJ analysis resulted in a lower SAC of 40%, which should translate to a smaller ACS of 44.1% (Figure 3.3.3c).

In Figure 3.3.4 we report the FFT and radial profile plot results for each batch of samples. The ethanol-related FFT image (Figure 3.3.4a) shows 3 low-definition rings, with no well-defined peaks being defined. This induces the information of low periodicity. Small and wide peaks (Figure 3.3.4b), with double than expected distances, show that the spacing is higher than it should be, with low-area uniformity.

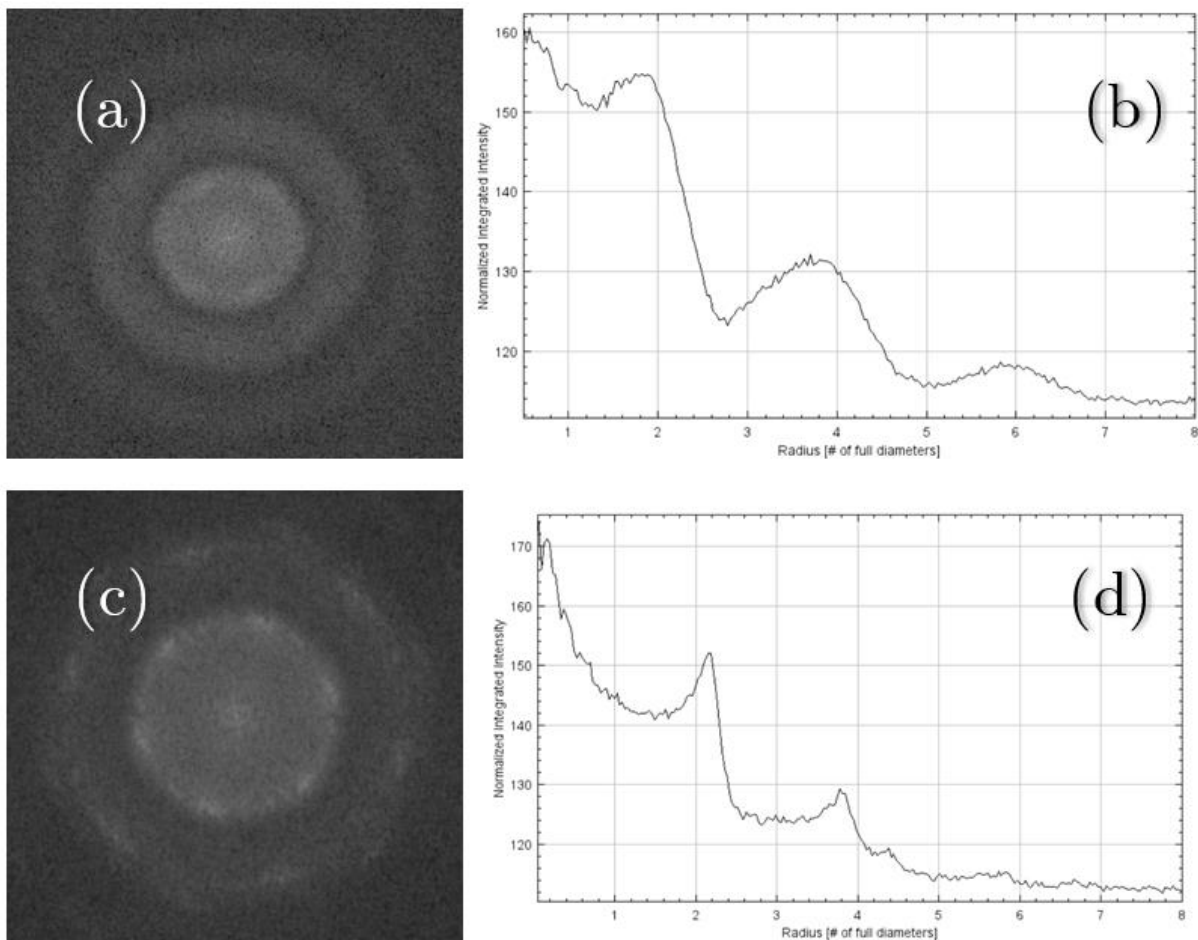


Figure 3.3.4 - Fast Fourier Transform of the SEM image and radial profile for each solvent for  $0.6 \mu\text{m}$  PS nanospheres depositions - ethanol (a,b) and diacetone (c,d).

For the diacetone sample, decent peaks can be seen in the FFT image (Figure 3.3.4c), with only 2 visible rings. The same doubled intersphere distance is observed at its radial profile (Figure 3.3.4d), while the radial profile peaks tend to be thinner and higher – a sign of distance uniformity. This would mean that, in the diacetone sample, the polystyrene dispersion would be superior in uniformity and inferior in periodicity than in the ethanol sample.

According to these results, one can notice that the use of ethanol shows a significant uniformity throughout the deposited area, however large honeycomb beads could not be found. As far as the diacetone-based samples are concerned, at least half of its surface is high-ordered and the self-assembly seemed perfect, yet significant surface area uniformity could not be found.

### 3.3.3. Aqueous sub-phase composition variation

Although similar testing was completed and reported in Section 3.2.2., the same concentrations were tested in the LB trough aqueous sub-phase. The three showed similar self-assembly performance to the previously tested, however, substrate coverage and the quality of the array were now evaluated. This information is also sustained by the SEM imagery (Figure 3.3.5), as one can see a tendency in the decrease of the honeycomb structure quality with the SDS concentration increase.

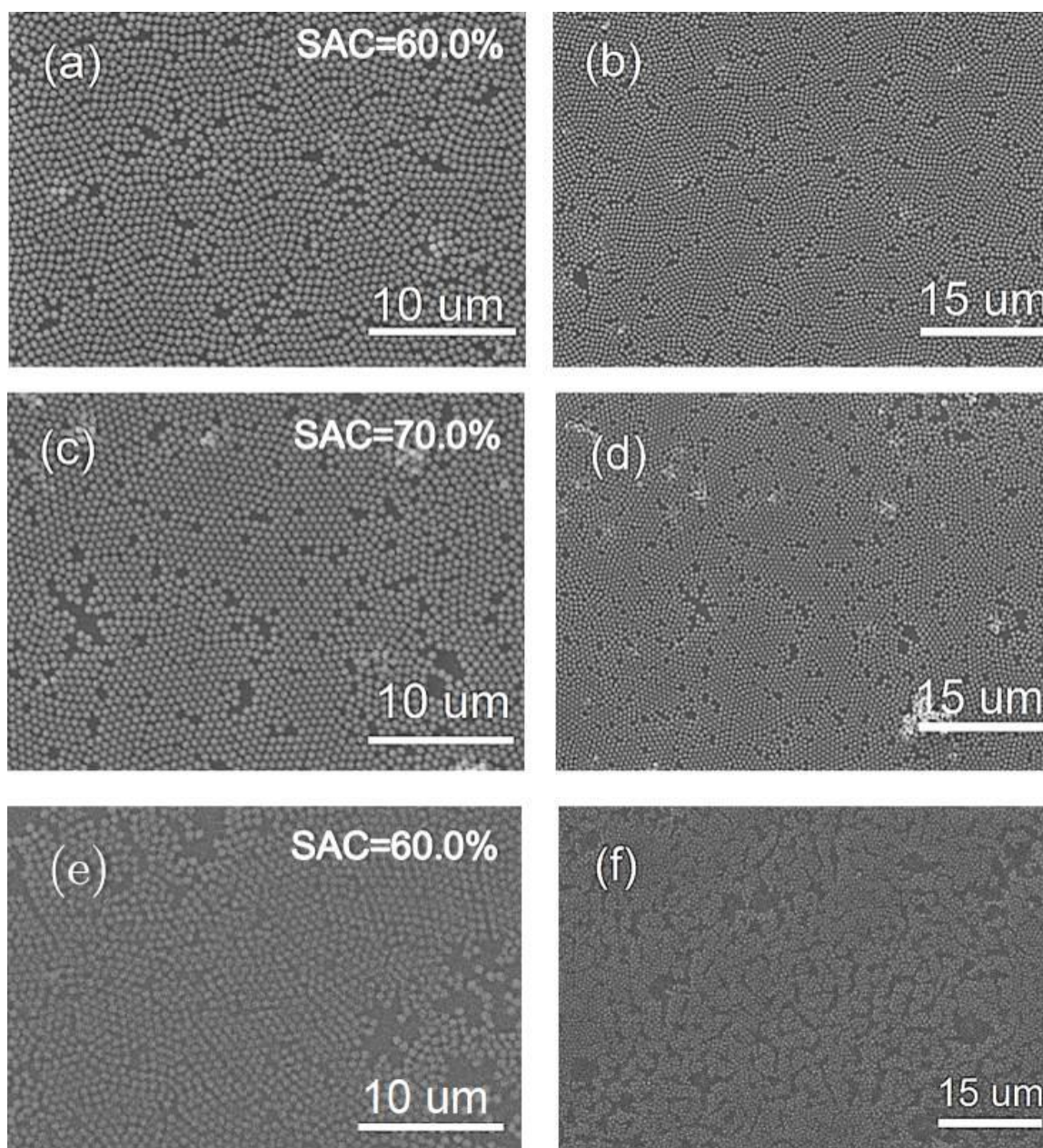


Figure 3.3.5 - SEM images of  $0.6 \mu\text{m}$  PS nanospheres depositions using a 1:3 proportion in ethanol for different SDS concentrations in the subphase, respectively: (a,b) 3 mg/l; (c,d) 4.5 mg/l; (e,f) 6 mg/l

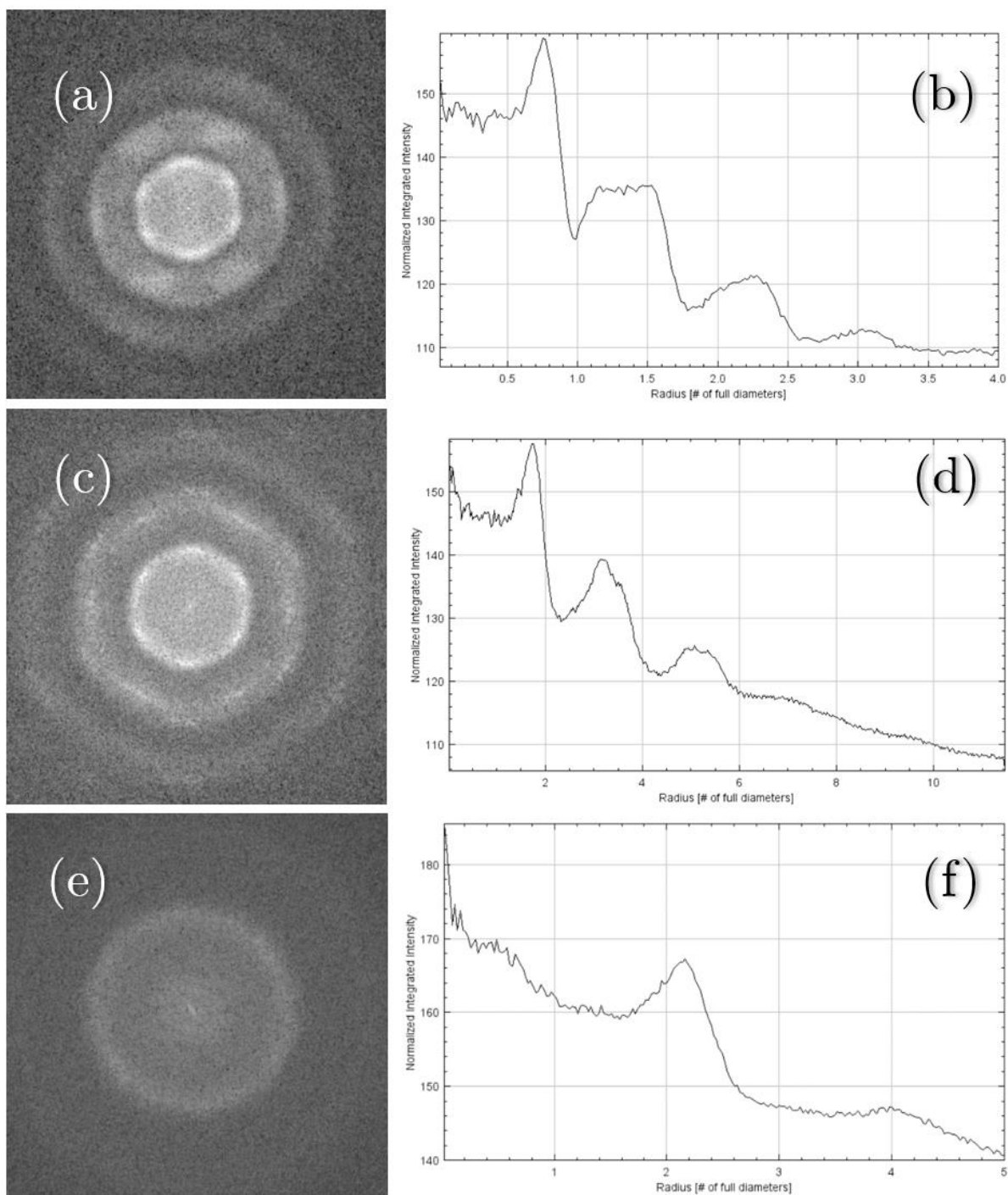


Figure 3.3.6 - Fast Fourier transform and radial profile of  $0.6 \mu\text{m}$  PS nanospheres depositions using a 1:3 proportion in ethanol for different SDS concentrations in the subphase, respectively: (a,b) 3 mg/l; (c,d) 4.5 mg/l; (e,f) 6 mg/l

The 3 mg/l concentration sample ImageJ analysis resulted in a SAC of 60%, which should translate to an ACS of 66.2% (Figure 3.3.5a). The FFT image (Figure 3.3.6a) shows 3 low-definition hexagonal rings, yet with no well-defined peaks being defined (Figure 3.3.6b). This induces the information of low periodicity. Concerning the 4,5 mg/l concentration sample, the ImageJ analysis resulted in a similar SAC of 70%, which should translate to a smaller ACS of 77.2% (Figure 3.3.5c). Decent peaks can be seen in the FFT image (Figure 3.3.6c and d). Regarding the 6 mg/l concentration sample, the ImageJ analysis resulted in a SAC of 60%, which should translate to a lower ACS of 66.2% (Figure 3.3.5e). Low-resolution peaks can be seen in the FFT image (Figure 3.3.6e), showing decent periodicity. A small radial distribution peak is seen at a doubled position (Figure 3.3.6f).

As the concentration increases in value, the area uniformity increases while the periodicity quality tends to decrease. The three arrays that were described in Figure 3.3.6 shown light FFT peaks, which are adjusted to a periodic and high-ordered model. Therefore, one can notice that the use of an average concentration of SDS (4.5 mg/l) tends to produce better and higher-quality self-assembly monolayers.

Concerning the substrate transferal and deposition, the achieving of a full substrate deposition coverage was not guaranteed within the methods described above. Although the formation of a high-ordered monolayer was always reported while using the LB trough, the transferal to the substrate was not always successful as expected (see Figure 3.3.7). In some, the substrate would not be fully deposited while, in others, the film would too thin (displaying distant nanosphere clusters), while in most a striped deposition pattern would be observed (visible at close looking but could not be photographed). Therefore, additional strategies and parameters had to be optimized and developed to improve the substrate deposition quality and area uniformity.



*Figure 3.3.7 – Resulting typical defected substrates after the previous Langmuir-Blodgett 0.6  $\mu\text{m}$  PS nanospheres depositions: the achieving of a direction-oriented colorful pattern (see Google Drive video 8) areas indicate the attaining of a high-ordered layer, whereas ACS is higher; on the other hand, the more transparent/whitish areas indicate a low-quality deposition, which should reveal disordered nanosphere clusters, therefore, low substrate area uniformity.*

### 3.3.4. Optimizing the substrate deposition area coverage

An additional step was introduced at first to cover this issue. The next batches of samples were submitted to a sonication treatment with UV-Ozone equipment, as it is known to improve surface wettability. Two additional strategies were designed and employed to improve close-packing success among the whole area of the substrate. The first – strategy A – started with the full barrier closing, disrupting the forming monolayer. A slow opening was then performed, with the microsyringe addition of 1 ml of ethanol providing the formation of a stronger and brighter 2D film. The second - strategy B - was the deposition of the same 1 ml of ethanol just before the nanosphere solution deposition onto the air-water interface, as a dispersant underlayer. Both resulting structures are detailed below: Figure 3.3.8 shows the resulting deposited substrates and Figure 3.3.9 combines the SEM images on these substrates and further ImageJ analysis.

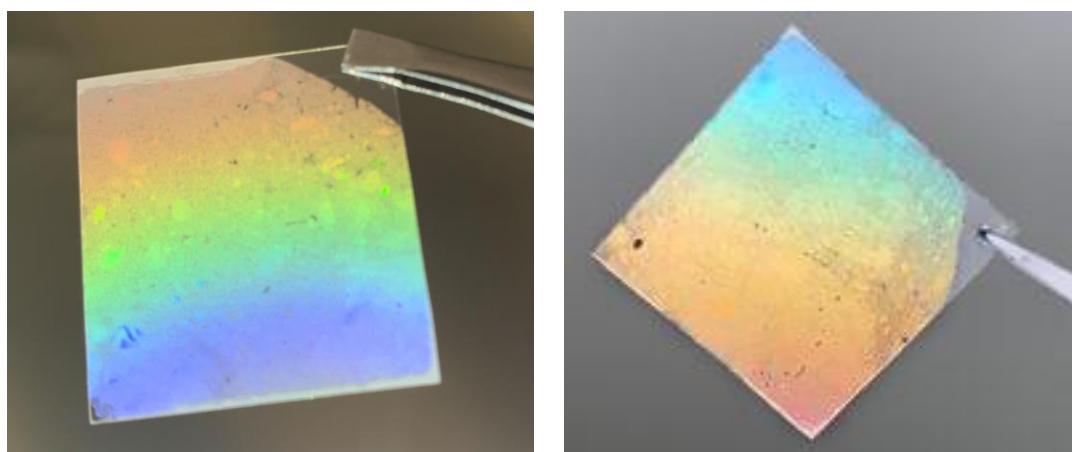


*Figure 3.3.8 - 0.6  $\mu\text{m}$  PS nanospheres deposited substrates for strategy A (left) and strategy B (right): both the full barrier closing and the use of an ethanol underlayer produce substrates that show remarkable higher deposition substrate deposition coverages, with reduced defect signs. – see Google Drive video 8*

Considering the sample produced via strategy A, the ImageJ analysis resulted in a SAC of 75%, which should translate to an ACS of 82.7% (Figure 3.3.9a). On the other hand, the radial profile function (Figure 3.3.9f) shows 3 small peaks. Regarding the sample produced via strategy B, the ImageJ analysis resulted in a lower SAC of 45%, which should translate to a lower ACS of 50.0% (Figure 3.3.9c). No decent peaks could be found in either the FFT images (Figure 3.3.9e and g), showing weak periodicity. The radial profile plots (Figure 3.3.9f and h) show a more defined peak at strategy A, which could reveal better uniformity. Both strategies allowed for excellent substrate coverages (Figure 3.3.8). More area uniformity was achieved via strategy B, while better close packing was attained with strategy A.

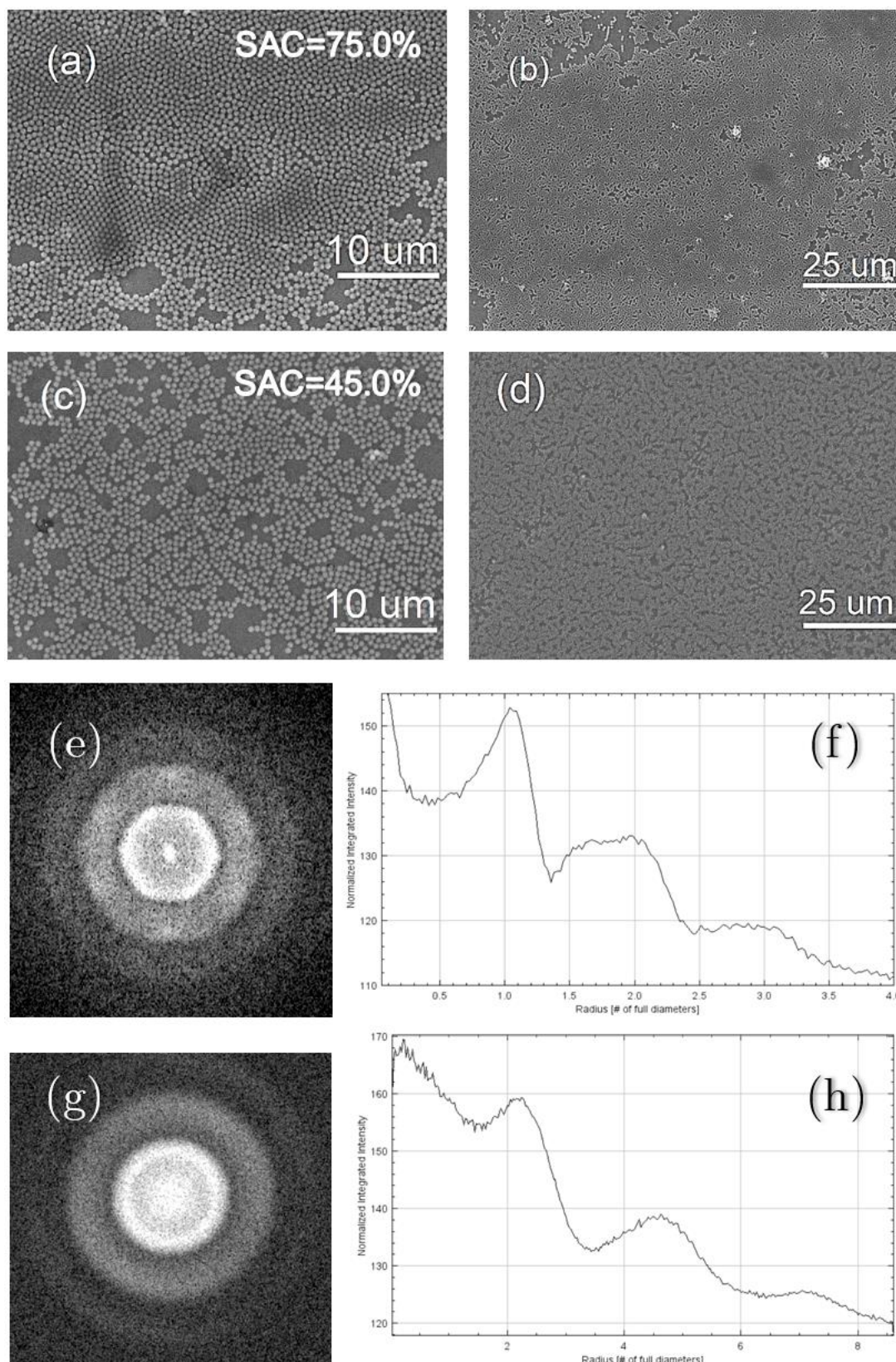


Figure 3.3.9 - SEM images, fast Fourier transform and radial profile plot of the two additional approaches, respectively: (a,b,e,f) strategy A - barrier closing variation and (c,d,g,h) strategy B - ethanol underlayer deposition - for 0.6 μm PS nanospheres depositions

### 3.4. Results Overview

In this section, we compile the previous results for further comparison and discussion, which will contribute to the optimization of the procedure depicted in Chapter II. An overarching Figure of Merit (FoM) was estimated by correlating the deposition results (Area Coverage Success - ACS, the number of FFT rings - FFT-R, and the Regularity Ratio - R [66]) with their relevance for future colloidal lithography applications.

Table 3.4.2 - Overall results and performance indicators attained within this work

Batch	ACS (%)	FFT-R (# of rings)	R (a.u.)	FoM (a.u.)
<b>PS Nanosphere Size Variation</b>				
0.6 $\mu\text{m}$	66.2%	3	73.3	84,0
0.7 $\mu\text{m}$	44.1%	3	32.0	24,4
0.9 $\mu\text{m}$	No decent deposition was observed.			
<b>PS Nanospheres Solvent Variation</b>				
Ethanol	55.1%	3	25.0	23,9
Diacetone	44.1%	2	72.0	44,9
<b>Aqueous Sub-Phase Composition Variation</b>				
SDS (3 mg/l)	66.2%	3	55.0	63,0
SDS (4.5 mg/l)	77.2%	3	42.0	56,2
SDS (6 mg/l)	66.2%	3	20.0	22,9
<b>Substrate Coverage Optimization Strategies</b>				
A. Full LB Closing	82.7%	3	37.5	53.7
B. EtOH Sublayer	50.0%	2	21.3	15.1

The regularity ratio was calculated for each batch recurring to equation (1) proposed by Stepniowski *et al.* (2014) [66], with  $I$  being the intensity of the corresponding highest peak in the radial function, and  $W_{1/2}$  is the width of the same radial function peak at half of its height. As a ratio between intensity and diameter-factor distances, its units are arbitrary (a.u.).

$$R = \frac{I}{W_{1/2}} \quad (1)$$

$$FoM = ACS * \sqrt{FFTR} * R \quad (2)$$

The overall quality of the resulting structures was quantified with the use of a global dimensionless FoM defined in equation (2), which merges the results in a way that the best performing structure is easily found and described. Within this work, we desire a high area coverage success ( $\sim 100\%$ ), a high number of FFT rings, and a high Regularity Ratio. While both the first and the third have a huge impact on the structure quality, the second could be seen as an indicative – bearing that in mind, different weights in the FoM expression were taken. Therefore, we propose a simple Figure of Merit (2) that evaluates the best performing batches.

The results displayed in Table 3.4.2 show how much the study parameters affected the quality and production of flexible nanosphere-coated substrates. The first aspect that can be perceived is that the use of this method suits better sizes of  $0.6\ \mu\text{m}$  than  $0.7$  or  $0.9\ \mu\text{m}$ . It is interesting to notice that the use of diacetone as a nanosphere solvent could improve the ordering of the monolayer, so it is an interesting choice for further testing. Regarding the SDS concentrations, there is a tendency in having better results in lower concentrations, however, for  $3\ \text{mg/l}$  and  $4.5\ \text{mg/l}$  the difference does not seem substantial. As time plays an important role in the stabilization of the monolayer, we would choose the later concentration as it tends to last a bit longer. When optimizing the substrate deposition coverage, an approach that includes the full closing of the LB barriers, followed by merging the resulting disrupted nanosphere clusters, is expected to introduce a brighter and stronger colloidal monolayer for further substrate transfers.

## Chapter IV: Conclusions and Future Perspectives

Within this work, an efficient approach for the self-assembly and deposition of 0.6  $\mu\text{m}$  polystyrene nanospheres on flexible substrates was successfully attained. This allows for the further development of colloidal lithography to produce more efficient photonic wavelength sized nanostructures. This experimental approach should provide for a remarkable photovoltaic performance boost in the upcoming years, as supported by previous simulation studies.

The use of a conventional Langmuir-Blodgett deposition method for larger nanospheres was optimized for lower sizes. Sodium dodecyl sulfate, at low concentrations in the aqueous sub-phase, proved to be an important third-party agent for the technique, as it was shown to allow nanosphere floatation and offer good self-assembly results. The use of ethanol as a colloidal solvent proved to be decent in quality, while its cost is quite low when compared to other possible solvents. A typical 1:3 proportion was also perceived as optimal for balancing both floatation improvement and fast sinking effects. Finally, when tested for different nanosphere sizes, this method showed better results for 0.6  $\mu\text{m}$  samples, decreasing with larger sizes (0.7 and 0.9  $\mu\text{m}$ ). The use of sodium chloride within the aqueous subphase to increase the subphase density and provide for a stronger air-water interface, reducing sinking effects, failed to produce any reasonable results.

As the stability of nanospheres in air-water assembly methods is naturally quite low, future works might be focused on the fine-tuning of the Langmuir-Blodgett trough controls, such as rest time, barrier/dipper moving rate, and temperature. The search for other solvents and anionic surfactants might also be important, however, as cost takes a huge part in the process, this might not be easy to achieve. A variation in the Langmuir-Blodgett aqueous sub-phase pH could also enhance close-packing, as proposed for spin-coating by Vogel *et al.* (2011).

Other dip coating methods could also be the subject of further studies, with the substrate tilt, speed rate, temperature, pH, and sub-phase composition taking a major optimization opportunity for the production of high-ordered arrays for photonic applications. Alternative sphere materials, such as silica, may introduce better uniformity results. Doctor blade (or blade coating) is also considered a primary alternative to Langmuir-Blodgett due to better scalability possibilities scalable and easier to employ at an industrial level. However, viscosity and thickness may constitute a further barrier to the production of better-quality films.



## References

1. Mendes, M.J. et al. Wave-optical front structures on silicon and perovskite thin-film solar cells. In *Solar Cells and Light Management: Materials, Strategies and Sustainability*; ENRICH, F., RIGHINI, G.C., Eds.; Elsevier, 2020 ISBN 9780081027622.
2. Vicente, A. et al. Solar cells for self-sustainable intelligent packaging. *J. Mater. Chem. A* 2015, doi:10.1039/c5ta01752a.
3. Vicente, A.T. et al. Multifunctional cellulose-paper for light harvesting and smart sensing applications. *J. Mater. Chem. C* 2018.
4. Wang, Y. et al. Advanced colloidal lithography: From patterning to applications. *Nano Today* 2018.
5. Yu, Y. et al. Colloidal Lithography. In *Updates in Advanced Lithography*; 2013.
6. Ariga, K. et al. 25th Anniversary article: What can be done with the langmuir-blodgett method? Recent developments and its critical role in materials science. *Adv. Mater.* 2013.
7. Ye, X. et al. Monolayer colloidal crystals by modified air-water interface self-assembly approach. *Nanomaterials* 2017, doi:10.3390/nano7100291.
8. Vogel, N. et al. A convenient method to produce close- and non-close-packed monolayers using direct assembly at the air-water interface and subsequent plasma-induced size reduction. *Macromol. Chem. Phys.* 2011, doi:10.1002/macp.201100187.
9. Albrecht, J. The future role of photovoltaics: A learning curve versus portfolio perspective. *Energy Policy* 2007, doi:10.1016/j.enpol.2006.07.013.
10. SolarPower Europe *Global Market Outlook For Solar Power 2018 - 2022*; 2018;
11. Green, M.A. Commercial progress and challenges for photovoltaics. *Nat. Energy* 2016.
12. Dresselhaus, M.S. et al. Alternative energy technologies. *Nature* 2001.
13. Schmela, M. et al. Global Market Outlook For Solar Power 2020-2024. *SolarPower* 2020.
14. Yan, N. et al. Recent progress of thin-film photovoltaics for indoor application. *Chinese Chem. Lett.* 2020, doi:10.1016/j.ccl.2019.08.022.
15. Li, M. et al. Indoor Thin-Film Photovoltaics: Progress and Challenges. *Adv. Energy Mater.* 2020.
16. Lee, T.D. et al. A review of thin film solar cell technologies and challenges. *Renew. Sustain. Energy Rev.* 2017.
17. Edoff, M. Thin film solar cells: Research in an industrial perspective. In *Proceedings of the Ambio*; 2012.
18. Hoffmann, W. PV solar electricity industry: Market growth and perspective. *Sol. Energy Mater. Sol. Cells* 2006, doi:10.1016/j.solmat.2005.09.022.
19. Schuss, C. et al. Photovoltaic (PV) energy as recharge source for portable devices such as mobile phones. In *Proceedings of the Conference of Open Innovation Association, FRUCT*; 2017.

20. Águas, H. et al. Thin Film Silicon Photovoltaic Cells on Paper for Flexible Indoor Applications. *Adv. Funct. Mater.* 2015, doi:10.1002/adfm.201500636.
21. Chapa, M. et al. All-Thin-Film Perovskite/C-Si Four-Terminal Tandems: Interlayer and Intermediate Contacts Optimization. *ACS Appl. Energy Mater.* 2019, doi:10.1021/acsaem.9b00354.
22. Shockley, W. et al. Detailed balance limit of efficiency of p-n junction solar cells. *J. Appl. Phys.* 1961, doi:10.1063/1.1736034.
23. Karg, M. et al. Colloidal self-assembly concepts for light management in photovoltaics. *Mater. Today* 2015, 18, 185–205.
24. Parchine, M. et al. Large area colloidal photonic crystals for light trapping in flexible organic photovoltaic modules applied using a roll-to-roll Langmuir-Blodgett method. *Sol. Energy Mater. Sol. Cells* 2018, doi:10.1016/j.solmat.2018.05.026.
25. Brongersma, M.L. et al. Light management for photovoltaics using high-index nanostructures. *Nat. Mater.* 2014.
26. Battaglia, C. et al. Light trapping in solar cells: Can periodic beat random? *ACS Nano* 2012, doi:10.1021/nm300287j.
27. Rim, S.B. et al. An effective light trapping configuration for thin-film solar cells. *Appl. Phys. Lett.* 2007, doi:10.1063/1.2789677.
28. Grandidier, J. et al. Solar cell efficiency enhancement via light trapping in printable resonant dielectric nanosphere arrays. *Phys. Status Solidi Appl. Mater. Sci.* 2013, doi:10.1002/pssa.201228690.
29. Haque, S. et al. Photonic-structured TiO<sub>2</sub> for high-efficiency, flexible and stable Perovskite solar cells. *Nano Energy* 2019, doi:10.1016/j.nanoen.2019.02.023.
30. Alexandre, M. et al. Optimum Luminescent Down-Shifting Properties for High Efficiency and Stable Perovskite Solar Cells. *ACS Appl. Energy Mater.* 2019, doi:10.1021/acsaem.9b00271.
31. Sanchez-Sobrado, O. et al. Photonic-structured TCO front contacts yielding optical and electrically enhanced thin-film solar cells. *Sol. Energy Mater. Sol. Cells* 2020, 196, 92–98, doi:10.1016/j.solener.2019.11.051.
32. Haque, S. et al. Design of wave-optical structured substrates for ultra-thin perovskite solar cells. *Appl. Mater. Today* 2020, doi:10.1016/j.apmt.2020.100720.
33. Torrisi, G. et al. Colloidal-structured metallic micro-grids: High performance transparent electrodes in the red and infrared range. *Sol. Energy Mater. Sol. Cells* 2019, doi:10.1016/j.solmat.2019.03.046.
34. Li, kezheng et al. Simple, yet mighty, principles to maximise photon absorption in thin media. *Optica* 2020, doi:10.1364/optica.394885.
35. Centeno, P. et al. Self-Cleaned Photonic-Enhanced Solar Cells with Nanostructured Parylene-C. *Adv. Mater. Interfaces* 2020, doi:10.1002/admi.202000264.
36. Ferry, V.E. et al. Light trapping in ultrathin plasmonic solar cells. *Opt. Express* 2010, doi:10.1364/oe.18.00a237.
37. Yao, Y. et al. Broadband light management using low-Q whispering gallery modes in

- spherical nanoshells. *Nat. Commun.* 2012, *3*, 1–7, doi:10.1038/ncomms1664.
38. Ye, X. et al. Two-dimensionally patterned nanostructures based on monolayer colloidal crystals: Controllable fabrication, assembly, and applications. *Nano Today* 2011, *6*, 608–631, doi:10.1016/j.nantod.2011.10.002.
  39. Sanchez-Sobrado, O. et al. Colloidal-lithographed TiO<sub>2</sub> photonic nanostructures for solar cell light trapping. *J. Mater. Chem. C* 2017, *5*, 6852–6861, doi:10.1039/c7tc01756a.
  40. Dimitrov, S.D. et al. Materials design considerations for charge generation in organic solar cells. *Chem. Mater.* 2014.
  41. Sanchez-Sobrado, O. et al. Lightwave trapping in thin film solar cells with improved photonic-structured front contacts. *J. Mater. Chem. C* 2019, doi:10.1039/c8tc06092d.
  42. Ober, C.K. et al. MONODISPERSED, MICRON-SIZED POLYSTYRENE PARTICLES BY DISPERSION POLYMERIZATION. *J. Polym. Sci. Polym. Lett. Ed.* 1985, *23*, 103–108, doi:10.1002/pol.1985.130230209.
  43. Shen, S. et al. Dispersion polymerization of methyl methacrylate: Mechanism of particle formation. *J. Polym. Sci. Part A Polym. Chem.* 1994, *32*, 1087–1100, doi:10.1002/pola.1994.080320611.
  44. Xia, Y. et al. Self-assembly approaches to three-dimensional photonic crystals. *Adv. Mater.* 2001, *13*, 409–413, doi:10.1002/1521-4095(200103)13:6<409::AID-ADMA409>3.0.CO;2-C.
  45. Hsieh, C.H. et al. Self-Assembled Mechanochromic Shape Memory Photonic Crystals by Doctor Blade Coating. *ACS Appl. Mater. Interfaces* 2020, doi:10.1021/acsami.0c07410.
  46. Yang, S.M. et al. Nanomachining by colloidal lithography. *Small* 2006, *2*, 458–475, doi:10.1002/smll.200500390.
  47. Kim, S.H. et al. Self-assembled colloidal structures for photonics. *NPG Asia Mater.* 2011.
  48. Hynninen, A.P. et al. Self-assembly route for photonic crystals with a bandgap in the visible region. *Nat. Mater.* 2007, *6*, 202–205, doi:10.1038/nmat1841.
  49. van Dommelen, R. et al. Surface self-assembly of colloidal crystals for micro- and nanopatterning. *Adv. Colloid Interface Sci.* 2018.
  50. Zhang, J. et al. Colloidal self-assembly meets nanofabrication: From two-dimensional colloidal crystals to nanostructure arrays. *Adv. Mater.* 2010, *22*, 4249–4269, doi:10.1002/adma.201000755.
  51. Yang, H. et al. Large-scale colloidal self-assembly by doctor blade coating. *Langmuir* 2010, doi:10.1021/la101721v.
  52. Birnie, D.P. Spin Coating Technique. In *Sol-Gel Technologies for Glass Producers and Users*; 2004.
  53. Corkery, R.W. Langmuir-Blodgett (L-B) multilayer films. *Langmuir* 1997, doi:10.1021/la9701743.
  54. Bardosova, M. et al. The langmuir-blodgett approach to making colloidal photonic crystals from silica spheres. *Adv. Mater.* 2010.
  55. Schwartz, D.K. Langmuir-Blodgett film structure. *Surf. Sci. Rep.* 1997,

doi:10.1016/s0167-5729(97)00003-4.

56. Açıkbaz, Y. et al. Characterisation of Langmuir-Blodgett films of new multinuclear copper and zinc phthalocyanines and their sensing properties to volatile organic vapours. *Sensors Actuators, B Chem.* 2007, doi:10.1016/j.snb.2006.11.004.
57. Huang, S. et al. Experimental conditions for a highly ordered monolayer of gold nanoparticles fabricated by the Langmuir–Blodgett method. *J. Vac. Sci. Technol. B Microelectron. Nanom. Struct.* 2001, doi:10.1116/1.1410943.
58. Hussain, S.A. et al. Unique supramolecular assembly through Langmuir – Blodgett (LB) technique. *Heliyon* 2018.
59. Retsch, M. et al. Fabrication of large-area, transferable colloidal monolayers utilizing self-assembly at the air/water interface. *Macromol. Chem. Phys.* 2009, doi:10.1002/macp.200800484.
60. Park, B. et al. Uniform two-dimensional crystals of polystyrene nanospheres fabricated by a surfactant-assisted spin-coating method with polyoxyethylene tridecyl ether. *Sci. Rep.* 2019, doi:10.1038/s41598-019-47990-z.
61. He, Y. et al. Surfactant-based promotion to gas hydrate formation for energy storage. *J. Mater. Chem. A* 2019, doi:10.1039/c9ta07071k.
62. Reynaert, S. et al. Control over colloidal aggregation in monolayers of latex particles at the oil-water interface. *Langmuir* 2006, doi:10.1021/la060052n.
63. Zhang, C. et al. Fabricating ordered 2-D nano-structured arrays using nanosphere lithography. *MethodsX* 2017, doi:10.1016/j.mex.2017.07.001.
64. Znamenskaya Falk, Y. et al. Langmuir – Blodgett monolayers of SBA-15 particles with different morphologies. *Microporous Mesoporous Mater.* 2018, doi:10.1016/j.micromeso.2017.07.049.
65. Tong, X. et al. Effects of nanoparticle coating on the adhesion of emulsion aggregation toner particles. *J. Adhes. Sci. Technol.* 2010, doi:10.1163/016942409X12541266699518.
66. Stępniewski, W.J. et al. Fast Fourier transform based arrangement analysis of poorly organized alumina nanopores formed via self-organized anodization in chromic acid. *Mater. Lett.* 2014, doi:10.1016/j.matlet.2013.11.099.
67. Alexander, J.K. et al. Electric field-induced astrocyte alignment directs neurite outgrowth. *Neuron Glia Biol.* 2006, doi:10.1017/S1740925X0600010X.
68. Chow, W.N. et al. Evaluating neuronal and glial growth on electrospun polarized matrices: Bridging the gap in percussive spinal cord injuries. *Neuron Glia Biol.* 2007, doi:10.1017/S1740925X07000580.
69. Kashi, M.A. et al. Optimum self-ordered nanopore arrays with 130-270 nm interpore distances formed by hard anodization in sulfuric/oxalic acid mixtures. *J. Phys. D. Appl. Phys.* 2007, doi:10.1088/0022-3727/40/22/025.
70. Noppakuadrattidej, P. et al. Importance of solvent singularity on the formation of highly uniform hexagonal close packed (HCP) colloidal monolayers during spin coating. *Colloids Interface Sci. Commun.* 2019, doi:10.1016/j.colcom.2019.100177.
71. Zheng, M. et al. Fabrication and structural characterization of large-scale uniform SnO<sub>2</sub>

- nanowire array embedded in anodic alumina membrane. *Chem. Mater.* 2001, doi:10.1021/cm010084q.
72. Moon, G.D. et al. Assembled monolayers of hydrophilic particles on water surfaces. *ACS Nano* 2011, doi:10.1021/nn202733f.



# Appendices

## A. ImageJ analysis

At first, one needs to import a high-resolution SEM image file (*File» Open...*) within the ImageJ user interface (Figure A.1). This image should be of such magnification that the spheres can still be visible, yet the structure is the biggest possible, otherwise, the analysis results, as radial function dependent, would tend to be quite small in resolution.

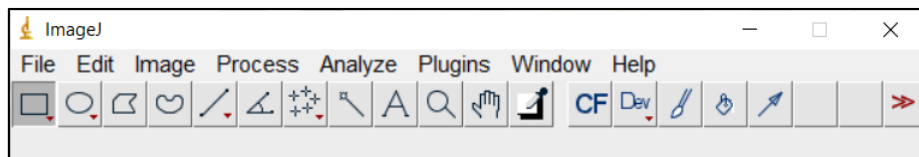


Figure A.1 - ImageJ user interface

When imported, the image needs to be treated to become a pure black and white array. To submit for further FFT and radial profile analysis, the scale should be converted in such a way that the abscises become related to the number of close-packed spheres (# of full diameters). By selecting the “*Straight*” selection tool and selecting a straight region on top of the SEM scale, one can go to “*Analyze» Set Scale*” and define the real size and its primary unit. Within this step, we selected a single sphere and modeled its real size as 0.3183 # of full diameters ( $0.3183=1/\pi$ ), to have diameter-based coordinates within the FFT image. The extraction of the radial profile from the FFT allows for a global measure, instead of selecting any specific circular region within the original SEM image. Therefore, we were in conditions to crop the resulting image (Figure A.2), by first selecting the desired area (with the selection tool “*Rectangle*” and then going to “*Edit» Crop*”).

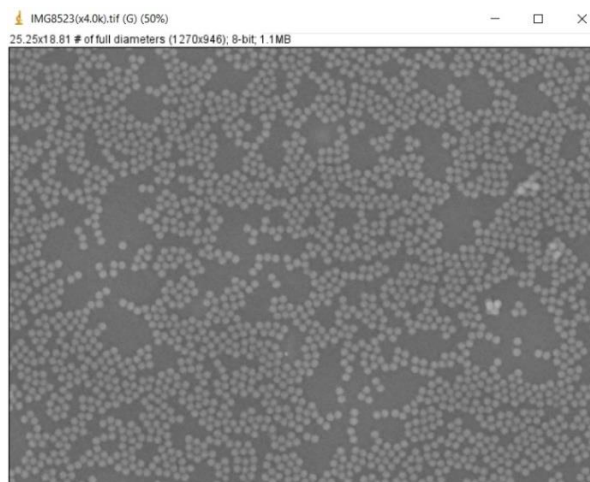


Figure A.2 - Cropped and scale SEM image in ImageJ

From now on, it is our goal to improve the SEM image in a way that single particles could easily be distinguished from the background surface and each other. The Image Type should be turned to 8-bit (“Image» Type» 8-bit”). For those matters, a combination of high contrast (“Image» Adjust» Brightness/Contrast...”) and image blur (“Process» Smooth”) should allow for the Image Threshold analysis (“Image» Adjust» Threshold...”). This analysis gives quantitative information on the surface area coverage (SAC) of nanospheres relative to the background area (Figure A.3).

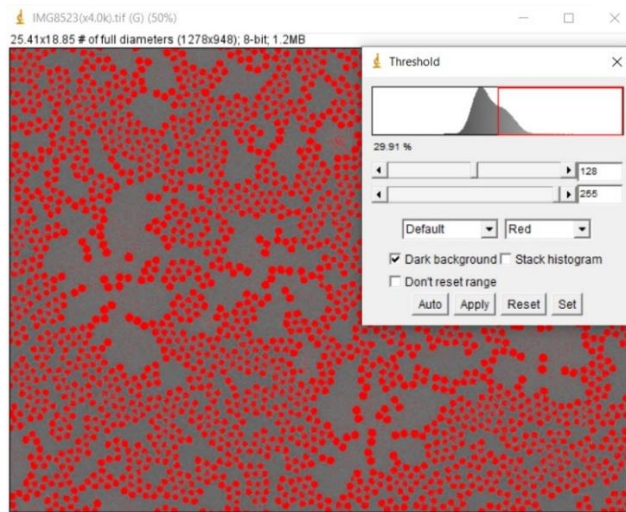


Figure A.3 - Image Threshold tool being performed onto the SEM image

After this analysis, and if the nanospheres are fully covered in a red overlay, one can press “Apply” to create a binary mask that turns the image to pure black and white (Figure A.4a). The Fast Fourier Transform (FFT) tool can then be applied (“Process» FFT» FFT”), providing a correspondent plot (Figure A.4b).

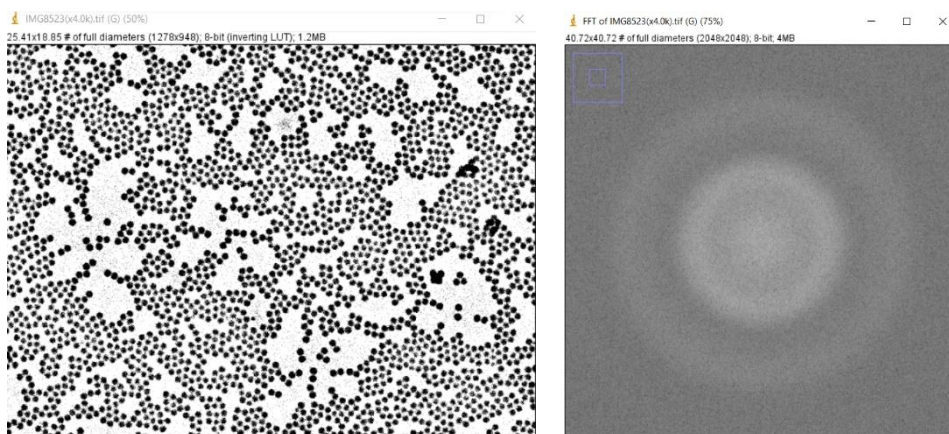


Figure A.4 - (a) Binary mask of the SEM image array; (b) Fast Fourier Transform of the same image

A Radial Profile plugin was downloaded ([Radial Profile Plot \(nih.gov\)](http://Radial Profile Plot (nih.gov))) and installed in ImageJ to perform the next step. Its application to the FFT image (“*Plugins*» *Radial Profile*”) produces a radial profile, a plot of normalized integrated intensities in the function of the distance as the number of full sphere diameters (Figure A.5). It is important to tick the box “*Spatial Calibration*” to guarantee the use of the scale and unit defined before. Regarding the function itself, the starting point is automatically defined as the center of the rectangle that bounds the image, but its position can be modified. The intensity at any given distance from the point represents the sum of the pixel values around a circle. This circle has the point as its center and the distance from the point as a radius. The integrated intensity is divided by the number of pixels in the circle that is also part of the image, yielding normalized comparable values. The profile x-axis can be plotted as pixel values or as values according to the spatial calibration of the input image, however, as defined in the scaling procedure, it is related to the diameter of the spheres for close-packing analysis.

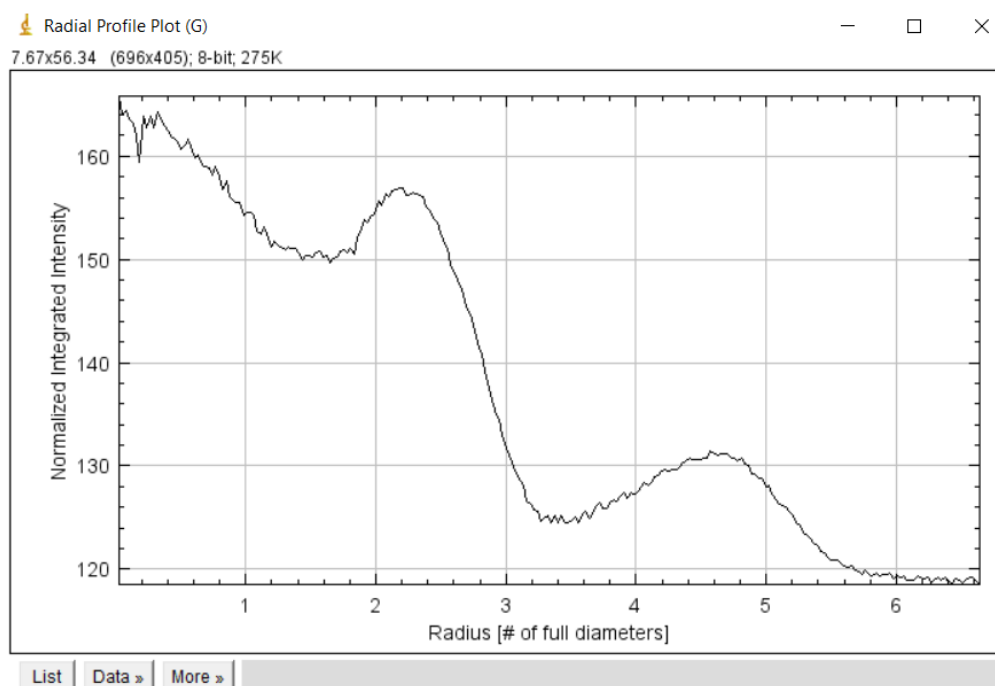


Figure A.5 - Radial profile plot: a plot of normalized integrated intensities in the function of the distance as the number of full sphere diameters